INL/RPT-24-80567 Rev. 0

Complete Development of Critical Capabilities for TRISO Fission Product Source Term Calculations and Quantify Mechanisms for Pd Penetration of SiC

August 2024

Technical Report

Jacob A. Hirschhorn[1], Ryan T. Sweet[1], and Stephen R. Novascone[1]

[1]Idaho National Laboratory

INL is a U.S. Department of Energy National Laboratory
operated by Batelle Energy Alliance, LLC

Complete Development of Critical Capabilities for TRISO Fission Product Source Term Calculations and Quantify Mechanisms for Pd Penetration of SiC

Technical Report

Jacob A. Hirschhorn[1], Ryan T. Sweet[1], and Stephen R. Novascone[1]

[1]Idaho National Laboratory

August 2024

Idaho National Laboratory
Computational Mechanics and Materials Department
Idaho Falls, Idaho 83415

http://www.inl.gov

Prepared for the
U.S. Department of Energy
Office of Nuclear Energy
Under U.S. Department of Energy-Idaho Operations Office
Contract DE-AC07-05ID14517

Page intentionally left blank

Abstract

Overall fission product (FP) release will be an important consideration for the licensing and deployment of advanced reactors utilizing tristructural isotropic (TRISO) fuels. This work focuses on enhancing and applying the BISON models needed to predict FP transport within TRISO particles and particle failure probability, both of which factor directly into release predictions. Specifically, this report details (1) the development of the models needed to predict palladium (Pd) conservation at the engineering scale and the application of those models to characterize Pd fluxes for input into a mechanistic multiscale model for Pd penetration; (2) the refinement of sorption mass transfer models and the development of models for trapping in porous layers, which were applied and compared to particle scans from AGR-2 to provide proof of concept for a method of particle-scale validation that may reduce uncertainties compared to compact-scale validation using data from integral effects tests; (3) the development of a failure-statistics-informed, mesh-independent methodology for applying smeared cracking, enabling further study of the localized multiphysics behaviors associated with cascading particle failure mechanisms; and (4) the preliminary characterization of those coupled multiphysics particle failure behaviors using smeared, nonretentive diffusivities to provide a baseline for future study and to guide ongoing engineering applications.

Page intentionally left blank

Acknowledgments

This report was authored by a contractor of the U.S. Government under contract DE-AC07-05ID14517. Accordingly, the U.S. Government retains a non-exclusive, royalty-free license to publish or reproduce the published form of this report, or allow others to do so, for U.S. Government purposes.

This research made use of the resources of the High Performance Computing Center at Idaho National Laboratory, which is supported by the DOE Office of Nuclear Energy and the Nuclear Science User Facilities under contract no. DE-AC07-05ID14517.

Page intentionally left blank

Contents

List of Figures

List of Tables

Acronyms

Ag	silver
AGR	Advanced Gas Reactor
Am	americium
C	carbon
Cs	cesium
CZM	cohesive zone modeling
EOL	end of life
EPMA	electron probe microanalysis
FCCI	fuel–cladding chemical interaction
FIMA	fissions per initial metal atom
FP	fission product
IAEA	International Atomic Energy Agency
INL	Idaho National Laboratory
IPyC	inner pyrolytic carbon
Kr	krypton
LANL	Los Alamos National Laboratory
LLS	lower-length scale
LWR	light-water reactor
MOOSE	Multiphysics Object-Oriented Simulation Environment
NEAMS	Nuclear Energy Advanced Modeling and Simulation
Np	neptunium
NRC	U.S. Nuclear Regulatory Commission
OPyC	outer pyrolytic carbon
ORNL	Oak Ridge National Laboratory
PARFUME	Particle Fuel Model
Pd	palladium
Pu	plutonium
PyC	pyrolytic carbon

ROM	reduced-order model
SiC	silicon carbide
Sr	strontium
TRISO	tristructural isotropic
U	uranium
UCO	uranium oxycarbide
UO_2	uranium dioxide
Xe	xenon
XFEM	extended finite element method

1. INTRODUCTION

The U.S. Nuclear Regulatory Commission (NRC) provides general guidance for the design and operation of nuclear power plants in the Code of Federal Regulations. This guidance was primarily written for monolithic light-water reactor (LWR) technology and has since been supplemented with guidance for small modular reactors and non-LWRs in a series of topical and other reports. Functional requirements, operational requirements, and fuel design criteria are developed for specific reactor and/or fuel designs to ensure that the NRC requirements are satisfied. The general purposes of each category are summarized in Table 1.1.

Table 1.1. General overview of functional requirements, operational requirements, and fuel design criteria.

Specification	General Purposes
Functional requirements	Maintain geometry, cooling, containment, and reloading capabilities
Operational requirements	Dictate power level, duty cycle, and performance requirements during normal and off-normal operations (qualitative)
Fuel design criteria	Establish reactor- and fuel-specific specifications to satisfy those specifications noted above (quantitative)

The overarching goals of the requirements include:

- Providing reactivity control
- Maintaining cooling
- Providing for fuel handling and storage
- Enforcing quality standards
- Recordkeeping
- Containing radioactive nuclides.

The last goal, containing radioactive nuclides, is the focus of this work in regard to tristructural isotropic (TRISO) fuel. TRISO fuel elements take the form of spherical pebbles or cylindrical compacts. Each graphitic fuel element contains thousands to tens of thousands of spherical TRISO particles. Each TRISO particle consists of a fuel kernel encapsulated in several structural and retentive layers. Figure 1.1 shows an example of a TRISO particle with its fuel

kernel, porous carbon buffer, inner pyrolytic carbon (IPyC), silicon carbide (SiC), and outer pyrolytic carbon (OPyC) layers [1]. All TRISO particles release some amount of fission product (FP)s, but failed particles release significantly more. A particle is generally considered to be failed when its SiC layer is compromised.

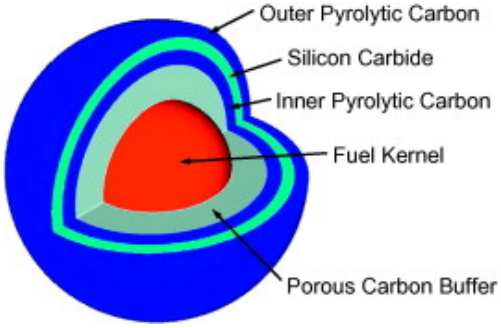

Figure 1.1. Example of a TRISO particle [1].

Any given reactor will contain many TRISO fuel elements, translating to a very large population of TRISO particles. Small variations in particle fabrication processes and conditions introduce statistically varying defects, which can contribute to particle failure. Due to the large population of particles and the dramatic impact of particle failure on FP release, one must calculate (1) how much radioactivity is released from both intact and failed particles and (2) the probability of failure in order to predict whether a given design will provide satisfactory containment of radioactive nuclides.

These calculations require the application of statistical methods and models for thermomechanical and thermochemical evolution at both the particle and fuel element scales. A full set of models has been implemented in the Multiphysics Object-Oriented Simulation Environment (MOOSE)-based BISON fuel performance code [2, 3]. The models were primarily adapted from the older Particle Fuel Model (PARFUME) TRISO fuel performance code [4] and have since been built on to improve performance and offer additional features.

BISON's TRISO predictions have been assessed against data from irradiation experiments conducted under the Advanced Gas Reactor (AGR) Program [5, 6, 7]. Trends in the comparisons are generally promising and consistent with our understanding of TRISO fuel system behavior, but there remains room for improvement. Subsequent sensitivity analyses and uncertainty quantification studies have indicated that errors in the BISON predictions arise from experimental noise, parameter uncertainties, and model form (i.e., missing physics) [8]. Follow-on modeling and simulation work has been conducted to address the last category. Examples include the development of sorption mass transfer models for the buffer-IPyC gap [7], microstructure-informed transport parameters for the SiC [9], and linear fracture mechanics-based failure models of retentive layers [10].

This work focuses on the development and implementation of additional high-impact physics models related directly to the containment of radioactive nuclides. The work is broken into four interrelated tasks:

1. Development of a mechanistic multiscale model for Pd penetration.
2. Refinement of the buffer-IPyC sorption mass transfer model and development of a model for trapping in porous layers, enabling particle-scale validation.

3. Application of spatially resolved smeared cracking methods to model statistical SiC failure, enabling the study of localized thermochemical failure behaviors.
4. Characterization of coupled thermochemical/thermomechanical particle failure behaviors.

These topics are covered in Section 2 through Section 5. Topic-specific summaries and conclusions are provided in each chapter. General conclusions and recommendations for future work are given in Section 6.

2. PALLADIUM PENETRATION MODEL

At elevated temperatures, Pd produced by fission in a TRISO kernel can migrate to the SiC layer, where it can react to form Pd-silicides with various stoichiometries in a process referred to as *Pd penetration* [11, 12]. The reaction is believed to proceed via slower solid-state and faster liquid-state mechanisms at lower and higher temperatures, respectively [13, 14]. The presence of silver (Ag) further complicates the phenomenon by decreasing the melting temperature of Pd, potentially increasing the range of temperatures over which the liquid-state mechanism dominates [13, 14]. Furthermore, differences in the solubility of Ag in the liquid phase and unreacted SiC are believed to contribute to increased Ag release from particles that have undergone Pd penetration [15].

The SiC layer is the primary structural layer in a TRISO particle. It is primarily responsible for the retention of metallic FPs and supporting the surrounding pyrolytic carbon (PyC) layers, which help to retain gaseous FPs. Pd penetration effectively thins the SiC layer, increasing stress and degrading its structural integrity. Pd penetration therefore represents an important fuel performance concern because it threatens the ability of TRISO particles to retain radioactive FPs.

TRISO particle failure is generally synonymous with *SiC failure*. Numerous models have been developed for the irradiation behaviors that can contribute to SiC failure, including IPyC and OPyC cracking and debonding, kernel migration, and Pd penetration. These have in turn been developed into a modular predictive framework for predicting TRISO particle failure and implemented in BISON as illustrated in Figure 2.1 [2, 3]. This work focuses on the Pd penetration portion of that framework, highlighted in green.

BISON currently models Pd penetration using an empirical correlation within the `PdPenetration` postprocessor class [16]. The correlation predicts the Pd penetration rate $\dot{P}_{Pd}$ in μm/day using:

$$\dot{P}_{Pd} = 38.232 \exp\left(\frac{11342.3}{T_K}\right), \tag{2.1}$$

where T_K is the time-averaged temperature of the SiC in Kelvin. T_K is further defined as:

$$T_K = \frac{T + T_{old}}{2}, \tag{2.2}$$

where T and T_{old} are the spatially averaged temperatures of the SiC at the current and previous time steps in Kelvin,

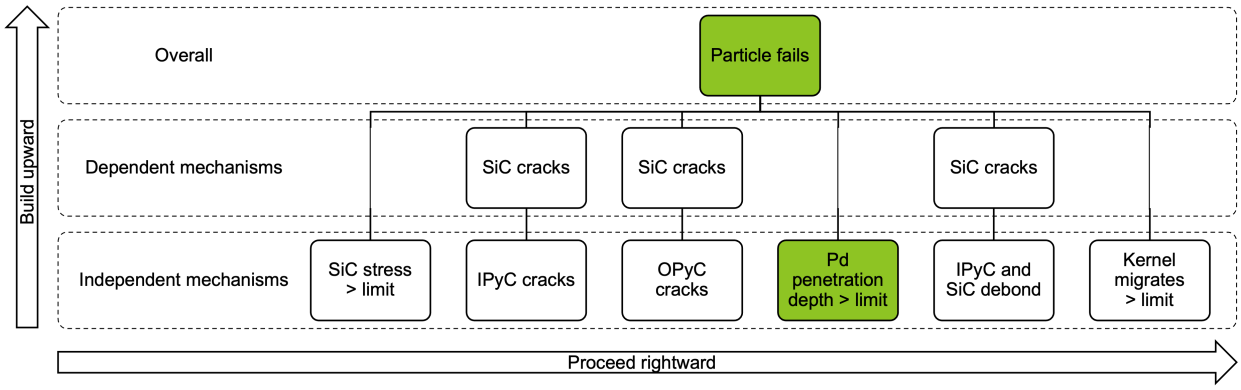

Figure 2.1. Block diagram illustrating how Pd penetration (green) impacts the predicted failure probability of TRISO particles in BISON.

respectively. An incremental formulation is then applied to calculate the total Pd penetration using:

$$P_{Pd} = P_{Pd,old} + \dot{P}_{Pd}\Delta t, \tag{2.3}$$

where Δt is the time step size in seconds, and P_{Pd} and $P_{Pd,old}$ are the total Pd penetration at the current and previous time steps in μm, respectively.

The Arrhenius coefficients used in the correlation were obtained by fitting to data from several irradiation experiments [16]. In doing so, implicit dependencies on particle operating conditions, material properties, and geometry were incorporated into the correlation. The correlation successfully reproduces the general thermal behavior of the data (i.e., higher temperatures correspond to higher rates of Pd penetration). However, the data exhibit considerable scatter. For a given temperature, observed Pd penetration depths vary by as much as two orders of magnitude. We can therefore expect that predictions obtained using the correlation could be inaccurate by orders of magnitude. This suggests that Pd penetration strongly depends on additional parameters.

A mechanistic multiscale Pd penetration model was developed to address the shortcomings noted above. The model was formulated such that it accounts for Pd production in the kernel, transport through various TRISO layers, and reaction with the SiC. These features incorporate explicit dependencies on:

- Operating conditions such as temperature and power density, including the effects of fuel depletion and breeding
- The transport properties of the individual layers
- Geometric considerations such as the thicknesses of individual layers, which vary over fuel life due to irradiation-induced swelling, densification, and/or anisotropic dimensional change.

Thus, the new model eliminates implicit dependencies on particle operating conditions and geometry that limit the applicability of the empirical correlation. These features allow the model to be applied more generally to support the

qualification and licensing of commercial TRISO designs that may not fall completely within the bounds of the existing irradiation database.

While ultimately implemented into BISON at Idaho National Laboratory (INL), the model relies heavily on components sourced from lower-length scale (LLS) simulations. Specifically, the engineering scale model incorporates diffusivities from atomistic studies conducted at INL and Los Alamos National Laboratory (LANL) and mesoscale studies conducted at INL. Interactions between these multiscale efforts are discussed in this report, and additional details regarding each effort can be found in complementary LLS milestone reports issued by each institution.

A block diagram illustrating the hierarchy of the multiscale Pd penetration model is shown in Figure 2.2, where LLS components are highlighted in green. In brief, a framework for modeling Pd conservation, including production, decay, and transport, was constructed at the engineering scale using parameters from the literature and atomistic simulations. A survey of literature from the AGR Program was then conducted to identify prototypic TRISO operating conditions. The conservation framework and operating conditions were then applied to characterize the Pd flux at the inner SiC surface. These data were supplied to the mesoscale team to inform the development of a mechanistic model for Pd penetration and corresponding reduced-order model (ROM). Finally, the ROM was implemented in BISON to complete the new engineering-scale Pd penetration model. Portions of the development and implementation process described above were iterative. For simplicity, this report focuses on the final results of the multiscale efforts.

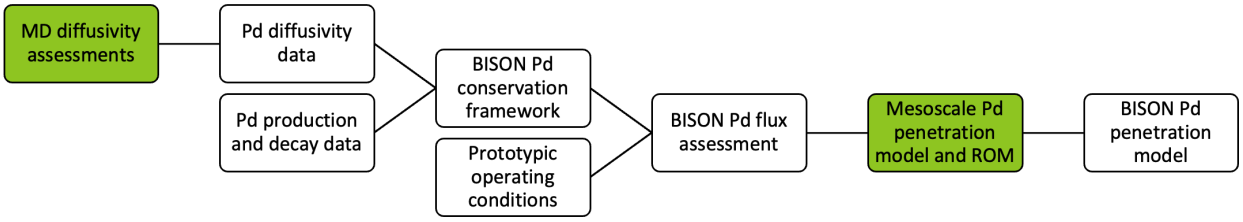

Figure 2.2. Block diagram illustrating how lower-length scale components (green) are incorporated into the engineering-scale Pd penetration model developed for BISON.

Conservation of Pd can be modeled by summing various production and loss terms according to:

$$\frac{\partial c}{\partial t} = \nabla \cdot D\nabla c + \dot{F}\gamma - \lambda c, \tag{2.4}$$

where c is the Pd concentration in mol/m^3, t is the time in seconds, D is the effective Fickian diffusivity in m^2/s, $\dot{F}$ is the fission rate density in fission/m^3·s, γ is the Pd fission yield in mol/fission, and λ is the Pd decay constant in 1/s.

Two additional Pd loss terms can be considered:

1. Release of free Pd from the TRISO particle, which is typically modeled by imposing a zero-value Dirichlet boundary condition at the outer surface of the OPyC. How this mechanism is modeled varies between simulations and is discussed in this report on a case-by-case basis.
2. Reaction of free Pd with the unreacted SiC and the subsequent formation of stable or metastable phases that limit further Pd transport. The development of a model for this mechanism and its implementation in BISON falls

within the scope of the mesoscale milestone at INL and is discussed mainly in a separate report.

The tasks illustrated in Figure 2.2 and the corresponding terms in Equation 2.4 effectively outline the remainder of this chapter. Power density and burnup govern the Pd source term while the influence of temperature dominates Pd transport. Prototypic TRISO operating conditions are discussed in Section 2.1, paving the way for a discussion focused on Pd production and decay in Section 2.2. Efforts related to modeling Pd transport within TRISO particles are then detailed in Section 2.3. An assessment of the expected Pd flux at the inner SiC surface was then conducted and is described in Section 2.4. The chapter concludes with a brief overview of the Pd reaction terms developed by the mesoscale team, a summary of conclusions related to the Pd penetration portions of this report, and a list of recommendations for future work.

2.1 Prototypic TRISO Operating Conditions

TRISO-based fuels are currently slated for use in numerous commercial reactor designs. Particle dimensions, compact form and dimensions, operating conditions, and duty cycle are expected to vary between applications. However, the majority of designs are expected to fall within or near the parameter space explored by irradiation experiments conducted under the U.S. AGR Program. The new Pd penetration model was developed with this nonproprietary parameter space in mind, allowing for reasonable deviations from the AGR design. Additional modifications and extensions required to target specific applications will be made in the future as needed.

Specific design parameters and operating conditions of interest include particle geometry, material composition, power density, temperature, and burnup. These parameters for the uranium oxycarbide (UCO)-fueled particles used in the AGR experiments AGR-1 [17], AGR-2 [18], and AGR-5/6/7 [19] are summarized in Table 2.1. AGR experiment AGR-3/4 was omitted because its purpose differed fundamentally from those of the other fuel-qualification-focused experiments [20]. Similar analyses will be made for uranium dioxide (UO_2)-fueled particles in the future as needed. These parameters were used to establish a representative particle design and operating condition ranges for use in the Pd flux assessment discussed later in this chapter.

A BISON input file was created to model loosely coupled thermomechanical and thermochemical TRISO particle evolution using the selected geometry, composition, and operating conditions. Thermomechanics was modeled in the main-app using the BISON classes listed in Table 2.2 and material properties from the existing AGR-2 BISON assessment. Thermochemistry was modeled in a sub-app using the BISON classes and material properties described in Section 2.3. This loosely coupled approach allowed for the formation and evolution of the buffer-IPyC gap to be resolved in the thermomechanics simulation but not in the thermochemistry simulation. This approach was necessary because the data needed to model Pd sorption mass transfer across the gap are not yet available [7].

Table 2.1. Design parameters and operating conditions of interest for various AGR Program irradiation experiments and the representative particle design and operating condition ranges selected for the Pd flux assessment in this work. Values were omitted from the table if an experiment used the same value as the preceding experiment. FIMA denotes fission per initial metal atom.

Parameter	AGR-1 [17]	AGR-2 [18]	AGR-5/6/7 [19]	This Work
Kernel radius (μm)	175.0	212.5		212.5
Buffer thickness (μm)	100.0			100.0
IPyC thickness (μm)	40.0			40.0
SiC thickness (μm)	35.0			35.0
OPyC thickness (μm)	40.0			40.0
Kernel density (kg/m^3)	10,400			10,400
Enrichment (wt%)	19.8	14.0	15.5	14.0
C/U (atom ratio)	0.5	0.4		0.4
O/U (atom ratio)	1.5			1.5
U fraction (kg U/kg UCO)	0.870	0.885		0.885
Buffer density (kg/m^3)	950			950
IPyC density (kg/m^3)	1,900			1,900
SiC density (kg/m^3)	3,190			3,190
OPyC density (kg/m^3)	1,900			1,900
Particle aspect ratio (-)	1			1
Peak power density (GW/m^3)	2.69	2.03	3.66	2.03–2.69
Surface temperature limit (K)	1673	2073	2073	298–2073
Peak compact burnup (% FIMA)	19.60	13.15	15.26	0.00–20.00

Table 2.2. Thermomechanics models and associated BISON classes used for the Pd flux assessment in this work. IIDC denotes irradiation-induced dimensional change.

Model	BISON class(es)
Conservation of energy	`HeatConductionTimeDerivative`, `HeatConduction`, and `NeutronHeatSource`,
Conservation of momentum	`TensorMechanicsMasterAction`
Buffer-IPyC mechanical contact	`ContactAction`
Buffer-IPyC thermal contact	`GasGapHeatTransfer`
Layer density	`Density`
Layer thermal expansion	`ComputeThermalExpansionEigenstrain`
Layer elasticity	`ComputeIsotropicElasticityTensor`
Kernel thermal conductivity and specific heat	`UCOThermal`
Kernel burnup	`TRISOBurnup`
Kernel swelling	`UCOVolumetricSwellingEigenstrain`
Kernel fission gas release	`UCOFGR` and `PlenumPressureAction`
Buffer thermal conductivity and specific heat	`BufferThermal`
Carbonaceous layer creep	`PyCCreep`
Carbonaceous layer IIDC	`PyCIrradiationEigenstrain`
SiC thermal conductivity and specific heat	`MonolithicSiCThermal`
SiC creep	`MonolithicSiCCreepUpdate`
Fast-neutron flux	`FastNeutronFlux`

2.2 Source and Decay Terms

Existing BISON classes can be used to model the production of Ag, cesium (Cs), strontium (Sr), krypton (Kr), and xenon (Xe) using constants and simple correlations to burnup and/or enrichment, which were largely taken from the PARFUME TRISO fuel performance code [4]. A new Pd source term model was developed and implemented as part of the current work. A review of fission yield data resulted in two important observations relevant to Pd conservation in TRISO fuels [21]. First, there are seven stable or long-lived Pd isotopes: ^{102}Pd, ^{104}Pd, ^{105}Pd, ^{106}Pd, ^{107}Pd, ^{108}Pd, and ^{110}Pd. For the purposes of this work, all seven isotopes are assumed to be stable and chemically identical. Second, Pd yield depends strongly on which uranium (U) or plutonium (Pu) nuclides are undergoing fission. Fuel burnout and breeding must therefore be taken into account to accurately predict Pd production in TRISO fuels reaching burnups of up to 20% fissions per initial metal atom (FIMA).

The new Pd production model was implemented in the `PdSourceMaterial` material class. It applies one-group approximations and simplified transmutation chains to account for the effects of fuel burnout and breeding on the production rate density of Pd. The transmutation chain relevant to Pd production, which also includes neptunium (Np) and americium (Am), is shown below:

$$^{238}\mathrm{U} \xrightarrow{n,\gamma} {}^{239}\mathrm{U} \xrightarrow{\beta-} {}^{239}\mathrm{Np} \xrightarrow{\beta-} {}^{239}\mathrm{Pu} \xrightarrow{n,\gamma} {}^{240}\mathrm{Pu} \xrightarrow{n,\gamma} {}^{241}\mathrm{Pu} \xrightarrow{\beta-} {}^{241}\mathrm{Am} \tag{2.5}$$

TRISO particle irradiations are typically on the order of months to years. Both ^{239}U and ^{239}Np have short half-lives on the order of minutes and days, respectively. Conversely, the Pu isotopes have long half-lives on the order of tens of years to tens of thousands of years. Comparing the TRISO irradiation timescale to the half-lives of the radioactive nuclides allows the transmutation chain to be simplified considerably:

$$^{238}\mathrm{U} \xrightarrow{\sim n,\gamma} {}^{239}\mathrm{Pu} \xrightarrow{n\gamma} {}^{240}\mathrm{Pu} \xrightarrow{n,\gamma} {}^{241}\mathrm{Pu} \tag{2.6}$$

Nuclide-specific Pd fission yields are summarized in Table 2.3 [21].

Table 2.3. Pd fission yields for selected fissile/fissionable nuclides [21].

Nuclide	Fractional Pd Yield (-)
^{235}U	0.0158
^{238}U	0.0874
^{239}Pu	0.1581
^{240}Pu	-
^{241}Pu	0.2451

Assuming that initially no Pu is present, and given the initial fuel density ρ, mass fraction of U in the fuel f_U, and

initial ^{235}U enrichment ϵ, the initial number densities N_i of ^{235}U and ^{238}U can be calculated using:

$$N_i = \begin{cases} \dfrac{\epsilon \rho f_U N_A}{M_i}; & ^{235}\text{U}, \\ \\ \dfrac{(1-\epsilon) \rho f_U N_A}{M_i}; & ^{238}\text{U}, \end{cases} \tag{2.7}$$

where N_A is Avogadro's number, and M_i is the molar mass of the nuclides.

`PdSourceMaterial` then uses a provided fission rate density $\dot{F}$ and the microscopic cross sections for fission σ_f^i and neutron capture σ_c^i to explicitly model the evolution of the ^{235}U, ^{238}U, ^{239}Pu, ^{240}Pu, and ^{241}Pu number densities over time. At each time step, a representative flux ϕ is calculated using:

$$\phi = \frac{\dot{F}}{\sum_{i=1}^{M} N_i^{\text{old}} \sigma_f^i}, \tag{2.8}$$

where M is the number of fissile/fissionable nuclides being considered (5), and N_i^{old} is the number density of each nuclide evaluated at the previous time step. The representative flux is then used to calculate fission densities F_i, capture densities C_i, and production densities P_i:

$$F_i = N_i^{\text{old}} \phi \sigma_f^i \Delta t, \tag{2.9}$$

$$C_i = N_i^{\text{old}} \phi \sigma_c^i \Delta t, \tag{2.10}$$

$$P_i = \begin{cases} 0; & i \leq 2, \\ C_{i-1}; & i > 2. \end{cases} \tag{2.11}$$

Finally, the number densities at the current time step are calculated using:

$$N_i = N_i^{\text{old}} - F_i - C_i + P_i. \tag{2.12}$$

Cross sections were taken from Reference [22] and calibrated to match cumulative specific fission density calculations performed for the AGR experiment AGR-3/4 [23]. The number densities are then used to weight nuclide-specific Pd fission yields γ_i taken from Reference [21]. For each fissile/fissionable nuclide, its total Pd yield is taken to be the sum of its yields for all stable and long-lived Pd isotopes. The total Pd yield γ is calculated using:

$$\gamma = s \frac{\sum_{i=1}^{M} F_i \gamma_i}{\sum_{i=1}^{M} F_i}, \tag{2.13}$$

where s is an optional constant that can be applied to scale the total Pd yield. Finally, the Pd production rate density

$\dot{P}_{\mathrm{Pd}}$ (in mol/m^3·s) is calculated using:

$$\dot{P}_{\mathrm{Pd}} = \frac{\gamma \sum_{i=1}^{M} F_i}{N_A \Delta t}. \tag{2.14}$$

Note that while this model accounts for the effects of fuel burnout and breeding to deliver reasonable Pd production rate densities for prototypic TRISO geometries and operating conditions, it employs numerous assumptions and simplifications and relies on parameters calibrated to a limited dataset. The represenative flux, cross sections, and number densities associated with this model should be used with caution if applied to analyses outside the scope of Pd production in prototypic TRISO fuels. This model is not intended to take the place of proper neutronic and depletion calculations performed with realistic transmutation chains, energy-resolved flux spectra, and appropriate multigroup cross sections. Proper neutronics and depletion calculations could be performed to provide BISON source terms and flux values directly when high-fidelity multiphysics modeling is required.

Given the limitations noted above, development of a more generally applicable FP source term modeling approach was undertaken by a collaboration between the Nuclear Energy Advanced Modeling and Simulation (NEAMS) and AGR Programs. This approach couples BISON with the MOOSE-based neutronics and depletion code Griffin to model the evolution of fuel constituents and FPs. Preliminary higher-fidelity results are consistent with existing source terms (including the new Pd model) for experiment AGR-2. The new multiphysics approach, which is expected to deliver more realistic chemical and isotopic FP source terms, will be incorporated into this work and other follow-on BISON analyses as soon as possible.

A simple case based on the selected design parameters in Table 2.1 was created to demonstrate the basic operation of `PdSourceMaterial`. The case was run to 20% FIMA using the models listed in Table 2.2, a power density of 2.03 GW/m^3, and a surface temperature of 1500 K. The evolution of selected fissile/fissionable fuel nuclides predicted by `PdSourceMaterial` is shown in Figure 2.3. The effects of ^{235}U consumption and Pu breeding from ^{238}U are clearly visible as functions of burnup. In reality, operator action is required to adjust reactivity and maintain the desired power output in the presence of fuel burnout and breeding.

Fuel composition evolution resulted in time-varying Pd production due to the fuel nuclides' varying Pd yields, even at constant power, as shown in Figure 2.4. Pd production initially increased as Pu isotopes with higher Pd fission yields were bred from ^{238}U. Pd production then began to level off later in fuel life as the ^{235}U was depleted. These behaviors varied with initial fuel composition and irradiation conditions. Aspects of the behaviors were also accounted for in the burnup and/or enrichment dependencies incorporated into BISON's existing FP production correlations. The effects of Pd production are examined further in the Pd flux assessment after the last piece of the Pd conservation framework, Pd transport properties, is covered.

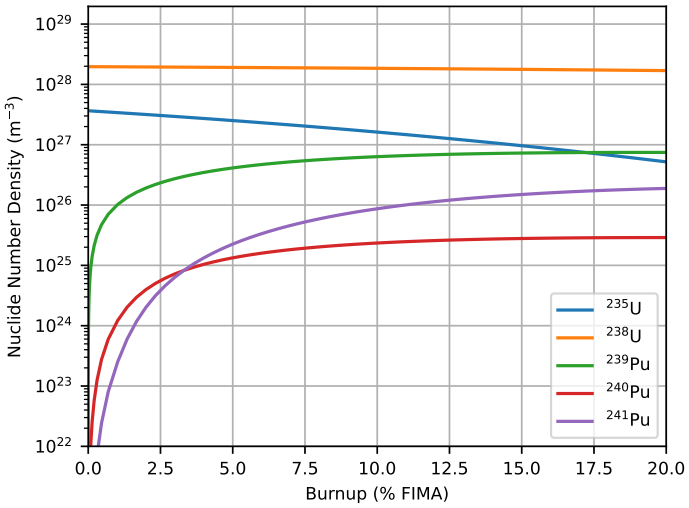

Figure 2.3. Evolution of selected fissile/fissionable fuel nuclides predicted by `PdSourceMaterial` showing fuel burnout and breeding.

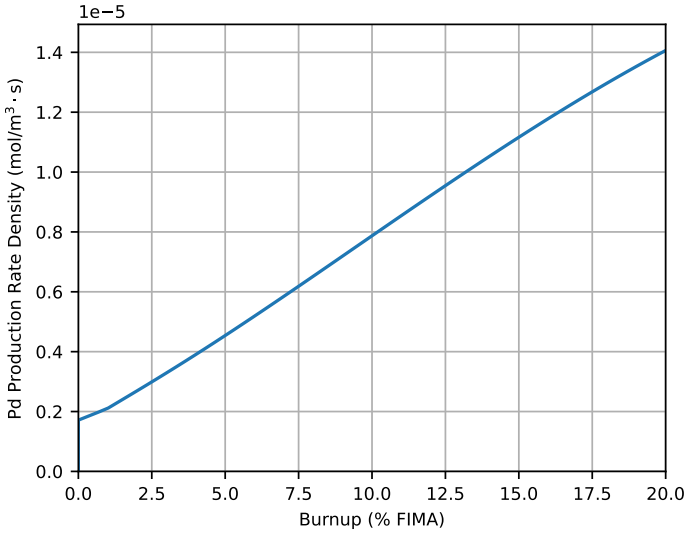

Figure 2.4. Evolution of Pd production predicted by `PdSourceMaterial` as a function of burnup. Pd production initially increases as Pu isotopes with higher Pd fission yields are bred from ^{238}U. Pd production begins to level off later in fuel life as the ^{235}U is depleted.

2.3 Transport

As noted in Equation 2.4, we assume that all Pd transport within TRISO particles can be modeled using effective Fickian diffusion. A literature search was conducted to obtain Pd diffusivities in the UCO kernel, buffer, IPyC, SiC, and OPyC,

but it yielded almost no useful data. The Ag diffusivities already used in BISON, which were primarily sourced from TRISO documentation issued by the International Atomic Energy Agency (IAEA), were therefore selected to model Pd transport due to the elements' proximity on the periodic table [24]. These values were supplemented with a preliminary model of the diffusivity of Ag in UCO, which is under development by the LLS team at LANL [25]. The diffusivities used to model Pd transport are summarized in Table 2.4 for reference.

Table 2.4. Ag diffusivities used to model Pd transport in the current work. The diffusivity in UCO was taken from the LLS team at LANL, a nonretentive value already used elsewhere in BISON was used for the buffer, and the remaining diffusivities were taken from IAEA values already used in BISON [24]. Here, R denotes the ideal gas constant in J/K·mol.

Layer	Diffusivity (m^2/s)	Source
UCO kernel	$D_0 + D_1 \exp(-Q_1/RT) + \frac{D_2 \exp(-Q_2/RT)}{1+D_3 \exp(-Q_3/RT)}$	[25]
	$D_0 = 8.5 \times 10^{-21}$	
	$D_1 = 1 \times 10^{-6}$	
	$Q_1 = 49 \times 10^3$ J/mol	
	$D_2 = 2 \times 10^9$	
	$Q_2 = 111.23 \times 10^3$ J/mol	
	$D_3 = 3.7 \times 10^{21}$	
	$Q_3 = 115 \times 10^3$ J/mol	
Buffer	1×10^{-8}	BISON nonretentive value
IPyC and OPyC	$D_0 \exp(-Q/RT)$	[24]
	$D_0 = 5.3 \times 10^{-9}$	
	$Q = 154 \times 10^3$ J/mol	
SiC	$D_0 \exp(-Q/RT)$	[24]
	$D_0 = 3.6 \times 10^{-9}$	
	$Q = 215 \times 10^3$ J/mol	

The selected diffusivities are plotted in Figure 2.5 for the range of particle surface temperatures specified in Table 2.1. The data illustrate how the constant buffer diffusivity contributes very little to Pd retention at any temperature. The SiC diffusivity is the lowest of the nonfuel layers at all temperatures, which is consistent with its role of being the primary retentive layer for metallic FPs. The data show that the PyC contributes less to Pd retention than the SiC, as expected.

The kernel diffusivity and its relationship to the SiC diffusivity at different temperatures are the most interesting aspects of the data. The inflection in the kernel diffusivity alludes to the different transport regimes captured by the LLS LANL model. The SiC diffusivity is lower up to about 1000 K (corresponding to one on the horizontal axis), where it crosses the kernel diffusivity. Pd transport is expected to be limited at these temperatures, and it would be expected that any Pd released from the kernel would be retained well by the SiC. At intermediate temperatures up to about 1350 K (about 0.75 on the horizontal axis), the kernel diffusivity remains about the same while the SiC diffusivity increases. Pd released from the kernel at these temperatures would be expected to be retained less well by the SiC.

Finally, the LLS LANL model predicts that the kernel diffusivity increases drastically beyond 1350 K. More and more Pd would be expected to be released from the kernel at these temperatures. The ability of the SiC to retain Pd is

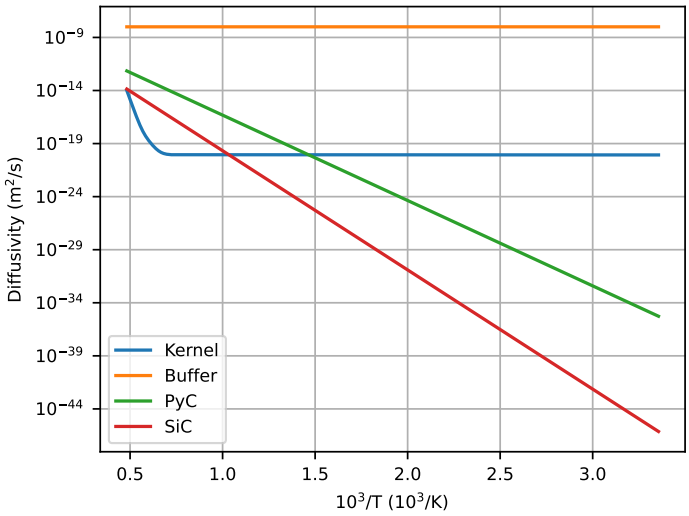

Figure 2.5. Diffusivities selected to model Pd transport in the current work.

most critical within this regime. These diffusivities complete the Pd conservation framework used in this work. These trends and the roles of the underlying properties are discussed further in the Pd flux assessment presented in the next section.

2.4 Flux Assessment

With all the terms needed by the Pd conservation framework in place, studies were conducted to characterize the expected Pd flux at the inner surface of the SiC for input into the mesoscale Pd penetration model. As mentioned above, Pd reaction with the SiC will ultimately be modeled using a ROM developed from the full LLS model. In the interim, a zero-value Dirichlet condition was imposed on the Pd concentration at the inner surface of the SiC to act as a surrogate for the reaction term. TRISO particle SiC layers are typically thin, and any reaction layer(s) that may form due to Pd penetration should also be thin. As such, changes in Pd flux due to the radial growth of the reaction layer were neglected. These approximations are expected to yield estimates that are sufficiently accurate to inform mesoscale model development.

Pd fluxes were first assessed using a constant power density of 2.03 GW/m^3 and particle surface temperatures ranging from 298 to 2073 K. All other design parameters and BISON models are listed in Table 2.1 and Table 2.2. The results, which appear to cluster at low and high temperatures, are plotted in Figure 2.6. The low-temperature cluster corresponds to a regime in which very little Pd leaves the kernel and migrates toward the SiC. The high-temperature cluster corresponds to a regime in which more Pd leaves the kernel and migrates more easily through the SiC.

In order to better illustrate these trends, instantaneous Pd fluxes at fuel end of life (EOL) were extracted from the simulations and are plotted as a function of particle surface temperature in Figure 2.7. The results clearly show the two regimes discussed above and the transition region between them, which is centered at about 1900 K for this particle

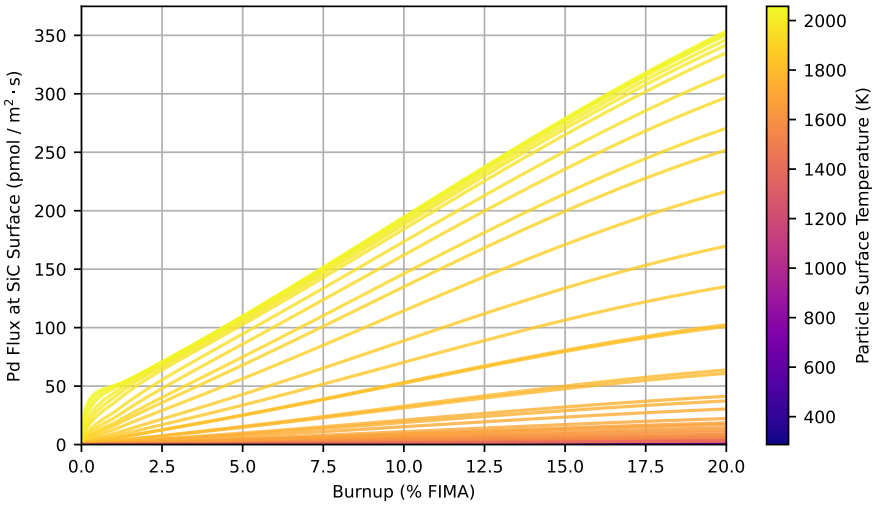

Figure 2.6. Predicted Pd fluxes at the inner surface of the SiC as functions of particle surface temperature and burnup.

design and these operating conditions. The upper plateau represents an estimate for the upper limit of Pd flux under accident conditions. The results show that Pd flux is highly sensitive to temperature as this limit is approached.

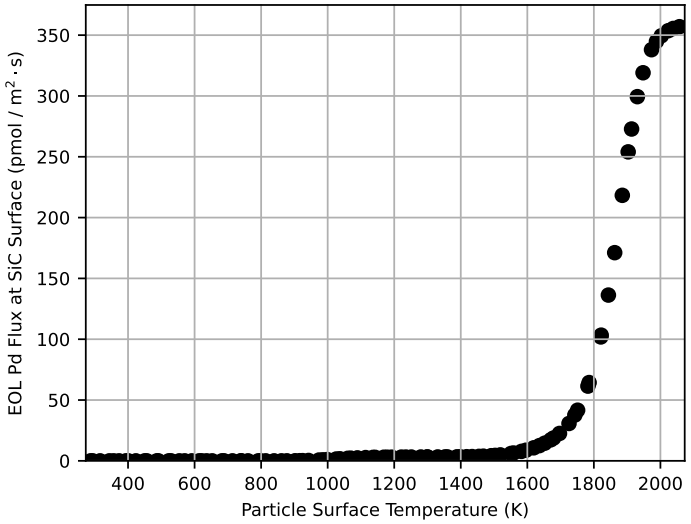

Figure 2.7. Predicted EOL Pd fluxes at the inner surface of the SiC as a function of particle surface temperature.

The current work and associated LLS efforts are focused more on normal operation than accident conditions. As such, the above data were replotted in Figure 2.8 to reflect a range of particle surface temperatures that are considered reasonable during normal operation. These results resolve two plateaus, which correspond more precisely to trends in the diffusivities plotted in Figure 2.5. At temperatures below about 900 K, little Pd escapes the kernel. From about

1200 to 1400 K, a moderate, nearly constant amount of Pd escapes the kernel and reaches the SiC. Finally, the Pd flux at the SiC increases rapidly beyond 1400 K. Figure 2.9 provides another view of these data, which resolves the predicted Pd flux over ranges of burnups and particle surface temperatures.

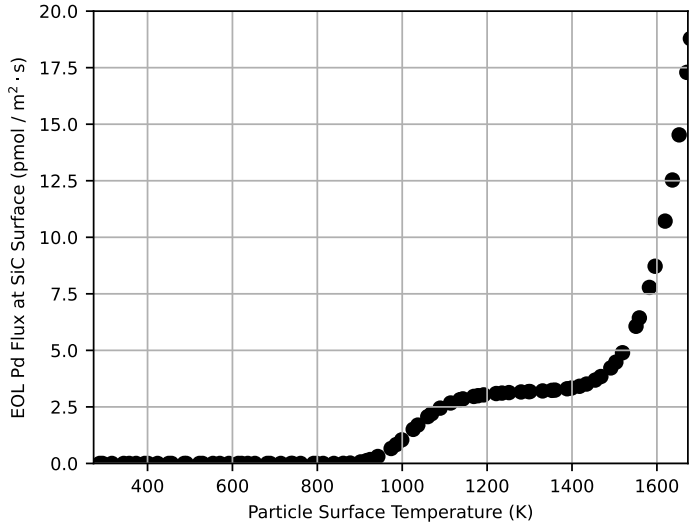

Figure 2.8. Predicted EOL Pd fluxes at the inner surface of the SiC as a function of particle surface temperature within the range of temperatures being considered for the development of the mesoscale Pd penetration model.

Pd fluxes were then assessed using power densities ranging from 2.03 to 2.69 GW/m^3. A constant particle surface temperature of 2073 K was selected from the highest plateau to limit Pd retention by the kernel and SiC, isolating the effects of power density. The results, which are plotted in Figure 2.10, are much more homogeneous than those obtained with variable particle surface temperatures. Pd fluxes at fuel EOL are plotted in Figure 2.11. These results reveal a nearly linear trend. As power increases, Pd production and the magnitude of the Pd concentration gradient increase, increasing Pd flux at the inner SiC surface.

Note that it is expected that a fission rate dependence will be incorporated into LANL's LLS diffusivity model [25]. The magnitude of this dependency's impact is currently not known, but it has the potential to affect the above results significantly. The Pd flux assessment will continue to be updated with new models and data as they are made available.

It is also worth noting that these two idealized surface temperature and power density cases do not necessarily reflect real-world fuel operation. Any period of low-temperature operation at power would promote the buildup of Pd within the kernel. It is plausible that a subsequent period of high-temperature operation could flush that Pd from the kernel, potentially yielding instantaneous Pd fluxes that are higher than those observed here. The authors recommend investigating this possibility for each specific fuel design/application.

Overall, the assessment shows that Pd flux depends on particle temperature strongly and in complex ways. Pd flux is estimated to be small below 900 K, be nearly constant at about 3 pmol/m^2·s from 1200 to 1400 K, and increase up to 20 pmol/m^2·s at the highest reasonable normal operating temperatures. The results suggest that Pd flux continues to increase toward an upper limit of 350 pmol/m^2·s under accident conditions. The flux varies approximately linearly

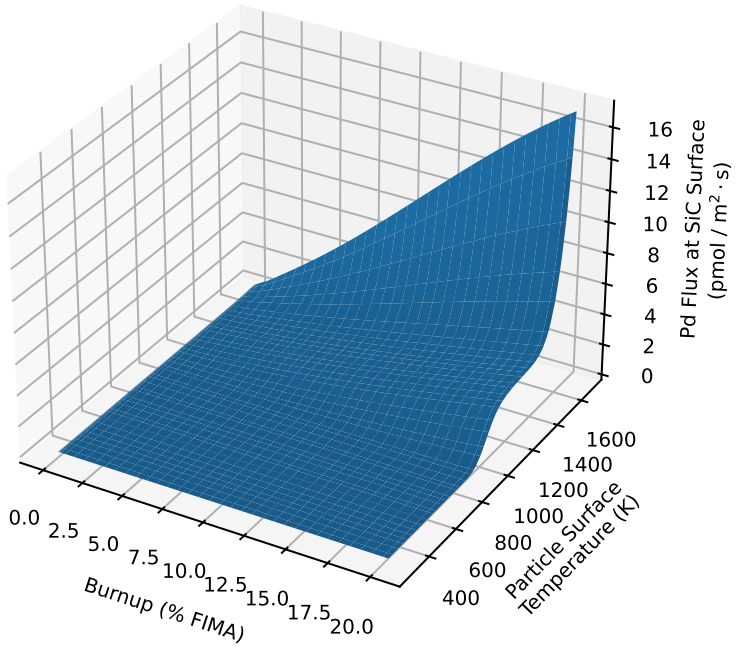

Figure 2.9. Predicted Pd fluxes over ranges of burnups and particle surface temperatures.

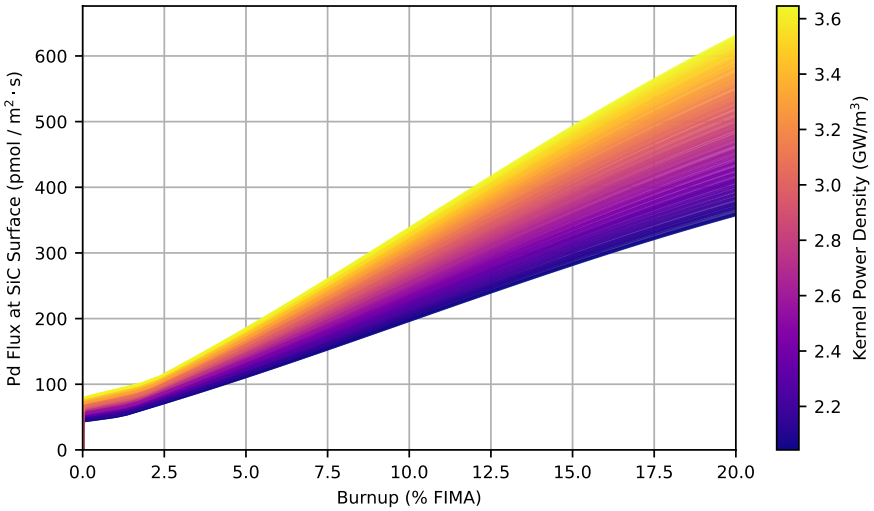

Figure 2.10. Predicted Pd fluxes at the inner surface of the SiC as functions of kernel power density and burnup.

with power density by a factor of up to about two. Periods of low-temperature operation followed by periods of high-temperature operation may lead to higher transient Pd fluxes.

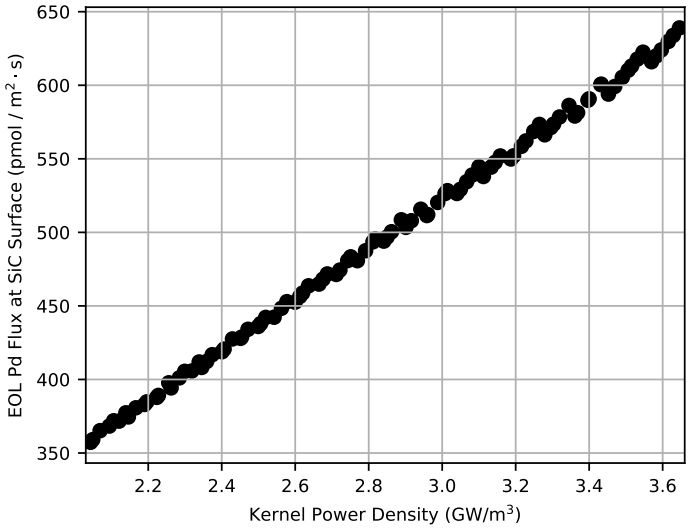

Figure 2.11. Predicted EOL Pd fluxes at the inner surface of the SiC as a function of kernel power density.

These observations are currently considered sufficient for the task of developing the mesoscale Pd penetration model. Additional analyses may be conducted in the future to better resolve the different physical regimes associated with normal operation versus accident conditions or solid-state versus liquid-state Pd attack. Evidently, Pd transport behaviors and therefore Pd penetration are highly sensitive to the diffusivities of Pd in the kernel and SiC. The authors recommend studies to reduce the substantial uncertainties in these parameters.

2.5 Reaction

The development and implementation of the Pd reaction term in BISON falls under the LLS milestone for Fiscal Year 2024. Complementary activities conducted to develop a mechanistic multiscale model for fuel–cladding chemical interaction (FCCI) in metallic fuels were conducted under the NEAMS Program during Fiscal Year 2023. These models and findings, which have already been incorporated into BISON, follow a similar FP production-transport-reaction modeling approach and are expected to expedite Pd penetration model development. Readers are encouraged to refer to the LLS milestone for more information.

2.6 Summary

At elevated temperatures, Pd produced by fission in a TRISO kernel can migrate to the SiC layer, where it can react to form Pd-silicides in a process referred to as *Pd penetration*. Pd penetration effectively thins the SiC, increasing stress, degrading its structural integrity, and threatening its ability to retain radioactive FPs. This process therefore has direct and detrimental impacts on the probability and severity of TRISO particle failure.

BISON currently models Pd penetration using an empirical correlation fit to average irradiation temperature. The correlation implicitly depends on particle operating conditions, material properties, and geometry. It does not explain any of the scatter found in the Pd penetration data from which it was derived, which can vary by up to two orders of magnitude at a given temperature. A mechanistic multiscale model for Pd penetration was developed through a NEAMS collaboration at INL and LANL to address these shortcomings and support the qualification and deployment of TRISO fuels for commercial applications.

The new model was formulated by explicitly considering Pd production within the kernel and transport through various particle layers under prototypic operating conditions, which were sourced from irradiation experiments conducted under the AGR Program. A new Pd source term model was developed and implemented to support the current work. It applies simplified transmutation chains and calibrated one-group cross sections to account for fuel composition evolution due to burnout, breeding, and their combined effects on overall Pd fission yield.

Due to a lack of Pd diffusion data for TRISO materials, Ag diffusivities from the literature and ongoing LLS work at LANL were used to approximate Pd transport behavior. The trends and magnitudes of the selected diffusivities are qualitatively consistent with expected metallic FP transport behaviors, but uncertainties associated with their use are considered high.

The resulting conservation framework and operating conditions were then applied to characterize the Pd flux at the inner SiC surface. Studies were conducted using representative particle dimensions and by varying either particle surface temperature or kernel power density. Overall, the assessment shows that Pd flux depends on particle temperature strongly and in complex ways. Pd flux is estimated to be small below 900 K, then be nearly constant at about 3 pmol/m^2·s from 1200 to 1400 K, and finally increase up to 20 pmol/m^2·s at the highest reasonable operating temperatures. The results suggest that Pd flux continues to increase toward an upper limit of 350 pmol/m^2·s under accident conditions. The flux varies approximately linearly with power density by a factor of up to about two. Periods of low-temperature operation followed by periods of high-temperature operation may lead to higher transient Pd fluxes.

Finally, these data and observations were delivered to the mesoscale team to inform the development of a mechanistic Pd penetration model and corresponding ROM for use in BISON. The development and implementation of the Pd reaction term in BISON falls under the LLS milestone for Fiscal Year 2024. Readers are encouraged to refer to the LLS milestone for more information. Future work in this area may include:

- Refining FP source term models, potentially leveraging ongoing BISON–Griffin multiphysics coupling work being pursued under a collaboration between the NEAMS and AGR Progams
- Incorporating more realistic Pd diffusivities as new experimental and/or LLS simulation data are made available
- Considering more realistic time-varying irradation conditions for characterizing the effects of transient operation on Pd transport
- Expanding the flux assessment to include Ag to enable the study of the liquid-state Pd-Ag-SiC attack mechanism.

3. TRANSPORT

Accurate models for intra- and interlayer FP transport within particles and accurate models for transport through the fuel element matrix are required to accurately predict radioactive nuclide release for TRISO fuel systems. Transport at the particle scale is typically modeled using effective Fickian diffusivities within layers. Until recently, interfaces between layers were assumed to be continuous, including across the buffer–IPyC interface, where a gap is known to form during irradiation. Particle release predictions were scaled up to estimate compact-scale release and then compared to results from integral effects irradiations conducted under the AGR Program. Shortcomings and challenges associated with this approach include the oversimplification of the transport physics at the buffer–IPyC interface and the large uncertainties that arise from comparing scaled particle-scale predictions to compact-scale experimental measurements.

The goals of this work include (1) improving FP release predictions by improving transport models at the particle scale and (2) reducing uncertainties by enabling a new pathway to validation at the particle scale. Two Cs electron probe microanalysis (EPMA) particle scans of an irradiated TRISO particle from the AGR experiment AGR-2 compact 2-2-3 are shown in Figure 3.1 [26]. The particle underwent partial buffer–IPyC debonding, and the two scans were oriented such that one traversed the bonded side (left) and the other traversed the unbonded side with the gap (right). The EPMA scans were used to guide model development in the current work.

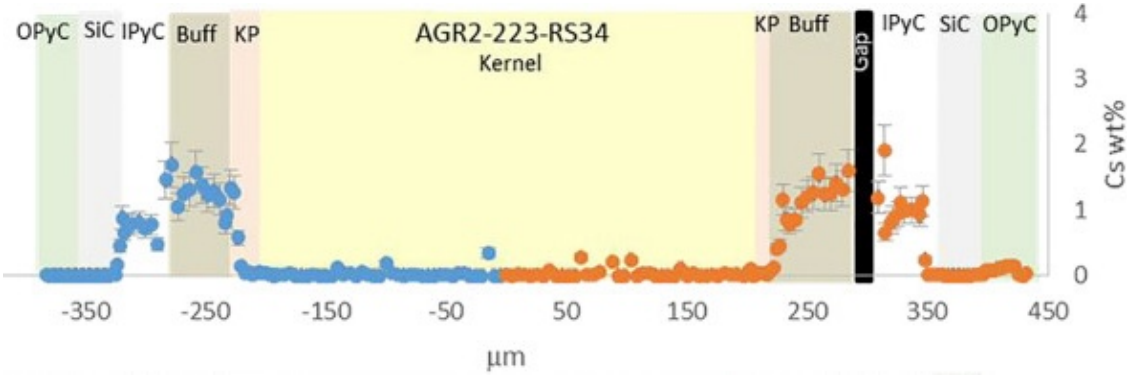

Figure 3.1. Two Cs EPMA particle scans conducted on an irradiated TRISO particle from the AGR experiment AGR-2 compact 2-2-3 [26]. The two scans were oriented in different directions within the particle, which underwent partial buffer–IPyC debonding.

The scans (in units of wt%) show a low Cs concentration in the fuel, which is more pronounced due to the high

density of the fuel relative to the surrounding layers. The Cs concentration is, on average, highest in the buffer and slightly lower in the IPyC. There is very little Cs in the SiC and OPyC, which is consistent with the SiC providing an effective barrier for the retention of FPs. Differences between the two scans are minimal, suggesting that the formation of the buffer–IPyC gap did not significantly limit Cs transport.

Similar scans are available for Sr, Ag, and other FPs, but they are not considered in this initial proof-of-concept work. Successfully simulating FP transport behaviors at the particle scale could help to motivate the collection of additional scans. These could then be used to validate the models and calibrate uncertain parameters such as diffusivities and sorption isotherm constants. A full set of physical transport models at the particle scale would enable the study of how particle deformation and damage impact FP release, laying the groundwork for additional thermomechanics enhancements and multiphysics analyses.

The existing AGR-2 BISON assessment was adapted so the experiment could be simulated and compared to the EPMA scans. The assessment uses time-varying compact-specific power densities and temperatures to simulate the particle irradiation history. Standard TRISO thermomechanics models and parameters used elsewhere in BISON, including mechanical and thermal contact at the buffer–IPyC gap, were incorporated into the 1D assessment to simulate the particle's behavior as realistically as possible.

Two behavioral model modifications motivated by the EPMA scans were made to reproduce the observed behaviors. These are detailed in Section 3.1 and Section 3.2. With the transport models in place, preliminary multiphysics simulations were conducted to begin to assess the relative impacts that various types of particle deformation and damage had on FP transport and release. These studies are presented in Section 3.3. Finally, the chapter concludes with findings related to the transport portions of this report and recommendations for future work.

3.1 Sorption Surface Conditions

Sorption mass transfer models were recently developed to more realistically model FP transport across the buffer–IPyC gap [7]. These were incorporated into the AGR-2 assessment to model Cs transport and attempt to reproduce the behaviors shown in the EPMA particle scans. A brief overview of the models is provided below to provide context for modifications made in the current work.

Sorption describes a set of physical processes in which a substance becomes attached to or unattached from the surface of another substance [7]. In the current context of an irradiated TRISO particle that has formed a buffer–IPyC gap, a FP may transition from the outer surface of the buffer to the gas-filled gap and then be deposited onto the inner surface of the IPyC. These two processes are frequently referred to as *adsorption* and *desorption*, respectively. Sorption isotherms are defined to express the partial pressure P of a species in a gas adjacent to a surface as a function of the concentration of the species at the surface c, the surface temperature T, and several experimentally measured constants [27]:

$$P = \exp\left(A + \frac{B}{T}\right) c^{\left(D + \frac{E}{T}\right)} + \exp\left[\left(A + \frac{B}{T}\right) + \left(D - 1 + \frac{E}{T}\right)(d_1 - d_2 T)\right] c, \tag{3.1}$$

where A, B, D, E, d_1, and d_2 are the sorption constants associated with the surface. The sorption constants used to model Cs transport in the current work are given in Table 3.1 [27]. The same values were applied to both the buffer and IPyC.

Table 3.1. Sorption constants used to model Cs transport in the current work [27].

Constant	Value
A	19.33
B	-47,290
D	1.518
E	4,338
d_1	3.397
d_2	6.15×10^{-4}

The implicit sorption model developed for BISON assumes that the partial pressure of each FP is uniform within the gap:

$$P_{\text{IPyC}} - P_{\text{buffer}} = 0. \tag{3.2}$$

This allows the relative FP concentrations at the two surfaces to be calculated from the surface conditions. An integral flux preservation constraint is applied to the two surfaces to conserve mass:

$$\int_{\Omega_{\text{IPyC}}} \mathbf{J}_{\text{IPyC}} \cdot \mathbf{n}_{\text{IPyC}} \, d\Omega_{\text{IPyC}} + \int_{\Omega_{\text{buffer}}} \mathbf{J}_{\text{buffer}} \cdot \mathbf{n}_{\text{buffer}} \, d\Omega_{\text{buffer}} = 0, \tag{3.3}$$

where Ω_i, $\mathbf{J_i}$, and $\mathbf{n_i}$ are the surface area, mass flux, and outward unit normal associated with surface i. Finally, each mass flux is further defined as:

$$\mathbf{J_i} = -D_i \nabla c_i, \tag{3.4}$$

where D_i is the diffusion coefficient of the FP in material i.

Sorption constants sourced from the literature are given in mmol of a FP per kg of carbon (C), whereas BISON simulations typically model FP concentrations in mol/m^3. The mass densities of the materials and unit conversion factors were applied to convert the BISON concentration for use in Equation 3.1. In our previous work, the bulk densities of the buffer and IPyC were used to make this conversion. This is a reasonable approximation for the IPyC because it is near its theoretical density, and its bulk density is therefore a good representation of its surface density.

This is not a good approximation for the low-density buffer, so a new approach was developed for the current work. Detailed characterization studies of unirradiated buffer materials were recently published [28]. The researchers found that the buffer, which is approximately 50% of its theoretical density, contains an average porosity of about 14%. This suggests that the density of the solid phase of the buffer is only a fraction of its theoretical density, perhaps due to disorder or material defects. For the purposes of this work, the porosity of the buffer is assumed to be isolated and to have no significant effect on the surface area that participates in sorption.

The density of the solid phase of the buffer ρ_s can be estimated from its overall density ρ and average porosity p using:

$$\rho_s = \frac{\rho}{1 - p}. \tag{3.5}$$

For values of $\rho = 1,050$ kg/m^3 and $p = 0.14$, the initial density of the solid phase of the buffer is estimated to be about

1,221 kg/m^3. BISON also includes models for buffer deformation during irradiation. The buffer tends to shrink as it densifies, pulling away from the IPyC to create a gap. The observed densification is assumed to happen at the expense of porosity. The `PorosityFromStrain` class was applied to account for these effects over the life of the particle.

The resulting model predicts that buffer porosity closes within the first 1% FIMA burnup for AGR-2. The predicted evolution of the buffer and IPyC densities is shown in Figure 3.2. Fluctuations in particle surface temperature manifest as small vertical features in the densities. Larger trends reflect the materials' responses to irradiation. The results show that the solid density correction is significant early in particle life.

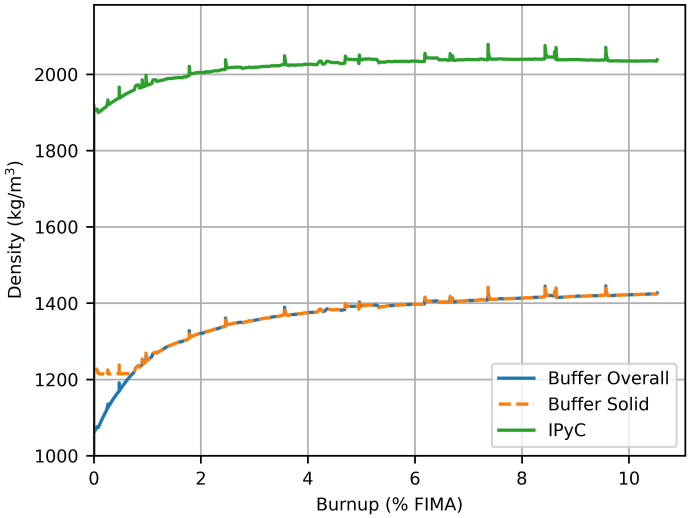

Figure 3.2. Predicted evolution of buffer and IPyC densities over time for AGR-2.

With the solid density correction in place, the model was used to predict the distribution of Cs within the particle. The EOL results are plotted in Figure 3.3 along with the data from the EPMA scans. To provide a clearer comparison, the horizontal axis of the simulation data was scaled linearly within each layer during postprocessing to match the layer dimensions and interface locations observed in the experiment. The buffer and SiC layers are shaded to facilitate discussions of Cs behavior across the particle radius.

As was mentioned above, there does not appear to be a significant difference between the EPMA scans taken from the bonded and unbonded sides of the particle. The BISON predictions are of the correct magnitude and generally consistent with the experimental data. BISON predicts a low concentration in the kernel, although the experimental data are still lower. BISON correctly predicts higher concentrations in the buffer and IPyC. The predicted IPyC concentration appears to be fairly accurate, but the predicted buffer concentration is significantly lower than that of the data. BISON predicts a rapidly decreasing concentration across the SiC and little to no concentration in the OPyC, which is consistent with the expected retentiveness of the SiC.

Overall, the trends in the simulation results are consistent with those in the experimental data, but there remains room for improvement. If a sufficient number of scans were available for different conditions, it could be possible to start calibrating diffusivities and sorption constants. For example, increasing the diffusivity in the fuel could lower

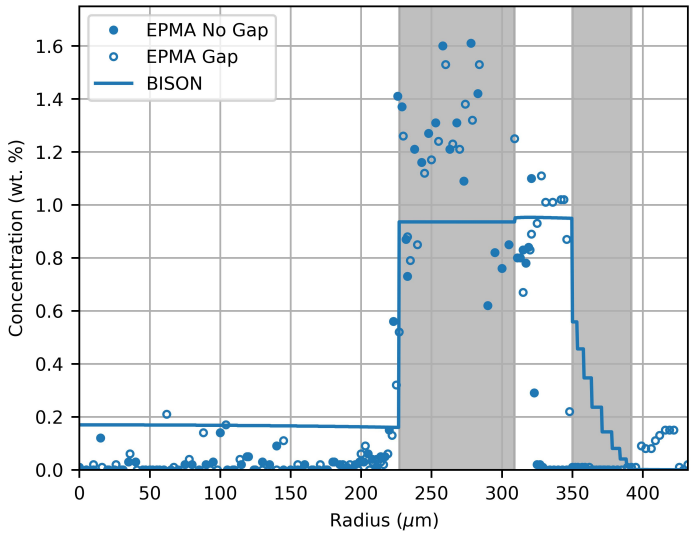

Figure 3.3. Comparison between the predicted EOL Cs distribution and the AGR-2 EPMA data.

the EOL concentration, improving agreement with the data. However, this seems premature due to the more drastic difference between the predicted and measured buffer concentrations, which appears to indicate a missing physical process.

The trapping of FPs in pores and defects has been observed in other fuel systems, such as the porosity that forms in metallic nuclear fuels. Given the low density of the solid phase of the buffer, even after densification, it is likely that it contains a significant population of defects that could trap FPs. A simple trapping model was developed to assess this hypothesis and evaluate whether its use improves the agreement between the predicted and measured Cs concentrations.

3.2 Trapping and Particle-Scale Validation

A simple FP trapping model was developed for the buffer to attempt to improve agreement between the predicted and measured Cs concentrations. This task was motivated by the goal of enabling parameter calibration and model validation at the particle scale. The authors emphasize that this behavior is hypothetical and the model is intended to serve only as a numerical tool to guide future model validation and other work. It should be used with caution until the behavior can be investigated experimentally.

Neglecting radioactive decay, Cs conservation is typically modeled by considering production, transport, and release according to:

$$\frac{\partial c}{\partial t} = \nabla \cdot D \nabla c + \dot{F} \gamma, \tag{3.6}$$

where c is the Cs concentration, t is the time, D is the effective Fickian diffusivity, $\dot{F}$ is the fission rate density, and γ is the Cs fission yield. The production term is applied only in the fuel while the transport terms are applied throughout

the particle. A zero-value Dirichlet boundary condition is typically applied at the outer surface of the OPyC to create a sink for Cs release.

In order to consider trapping, the Cs concentration was split into two quantities: the free Cs concentration c_F and the trapped Cs concentration c_T. The total Cs concentration c at any location is the sum of the two. All Cs produced by fission is initially free, and only free Cs is permitted to diffuse. Conservation of the two quantities is described by:

$$\frac{\partial c_F}{\partial t} = \nabla \cdot D \nabla c_F + \dot{F}\gamma - \dot{R_T} + \dot{R_F}, \tag{3.7}$$

$$\frac{\partial c_T}{\partial t} = \dot{R_T} - \dot{R_F}, \tag{3.8}$$

where $\dot{R_T}$ and $\dot{R_F}$ are the rate densities associated with trapping and untrapping (freeing), respectively.

The trapping rate is assumed to have an Arrhenius behavior described by:

$$\dot{R_T} = c_F \exp\left(\frac{-Q_T}{k_B T}\right), \tag{3.9}$$

where Q_T is the activation energy for trapping, k_B is the Boltzmann constant, and T is the temperature. Note that the trapping rate goes to zero as c_F goes to zero. A Q_T value of 2.3 eV was selected based on the activation energy for the diffusivity of Cs in the IPyC.

The freeing rate is also assumed to have an Arrhenius behavior described by:

$$\dot{R_F} = c_T \exp\left(\frac{-SQ_T}{k_B T}\right), \tag{3.10}$$

where S is a scalar value that represents the ratio of the activation energies for freeing and trapping. Values of S greater than one produce trapping (i.e., it is easier for a FP to become trapped than to escape from a trap). Similar to before, the freeing rate goes to zero as c_T goes to zero.

A S value of 1.01 yielded a reasonable agreement with the experimental data. This value corresponds to a situation where the potential barrier associated with escaping a trap is only 1% higher than the barrier associated with becoming trapped. The predicted Cs distribution is shown in Figure 3.4. The results show that the model produces trapping in the buffer, increasing the total Cs concentration, which is consistent with the average of the experimental data. There is a corresponding reduction in the concentration in the IPyC, and the other layers appear to be relatively unaffected.

These modifications are believed to complete the set of behavioral models needed to model FP transport at the particle scale. While trapping in the buffer remains hypothetical, including it as an option yields a flexible framework that delivers reasonable results when compared to the limited experimental data currently available. This opens up a new pathway to particle-scale calibration and validation, which could potentially lower uncertainties relative to compact-scale validation efforts. The authors recommend investigating these behaviors experimentally to guide model refinement and application. The authors also recommend the collection of additional particle-scale data. Individual particles could be irradiated at low temperatures to provide a known source of FPs. The particles could then be annealed to facilitate FP transport and scanned to be compared to model predictions. This approach would reduce uncertainties

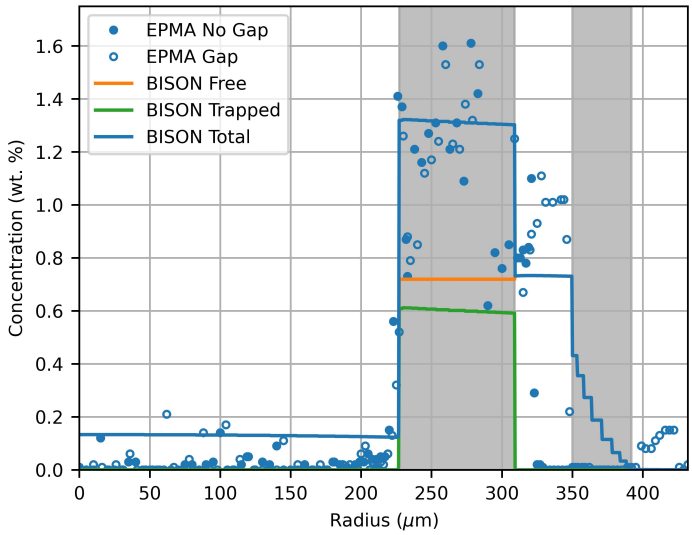

Figure 3.4. Comparison of the predicted EOL Cs distribution and the AGR-2 EPMA data when considering trapping in the buffer.

in power and temperature, allowing experimental conditions to be simulated more accurately. The approach would also eliminate uncertainties associated with particle failure, which could confound simulations involving compacts with unknown numbers of particle failures.

3.3 Preliminary Multiphysics

BISON currently leverages several different techniques to model the effects of particle damage on the thermomechanical state of its materials and FP transport and release. Major types of damage include (1) layer cracking, primarily of the IPyC and SiC, and (2) partial and full debonding of the buffer–IPyC and IPyC–SiC interfaces. The techniques applied to model the multiphysics effects of these behaviors are summarized in Table 3.2.

Table 3.2. Techniques currently applied to model the effects of particle damage on the thermomechanical state of its materials and FP transport and release.

Damage Behavior	Thermomechanical Approach	Thermochemical Approach
Layer cracking	Discretely meshed cracks	Smeared application of nonretentive diffusivities in the vicinity of the crack
Partial and full layer debonding	Discretely meshed interface discontinuities with thermal and mechanical contact constraints	Sorption mass transfer constraints

While a predefined discretely meshed layer crack is not useful for studying crack initiation and propagation behaviors, it is an effective tool for modeling the thermomechanical impact of an existing crack on the stress state of

surrounding materials. This has been a useful tool for modeling the likelihood of SiC failure given IPyC cracking. Modeling the statistical and spatial distributions of crack formation and evolution behaviors would also be beneficial for studying and predicting cascading particle failure behaviors. These topics are discussed further in the next chapter. The effects of layer cracking on FP transport and release are currently modeled in decoupled simulations by applying smeared, nonretentive diffusivities in the vicinity of prescribed cracks. This approach seems logical and may be a sufficiently accurate approximation of the real behavior, but it has not been investigated in detail and is not entirely consistent with the thermomechanical approach.

Sorption mass transfer models were applied to assess the appropriateness of this approach. IPyC cracks were chosen for study due to the magnitude of their influence on SiC mechanical behavior and therefore particle failure. The assessment aimed to answer this question: Is it sufficient to model sorption mass transfer to the inner surface of the cracked IPyC where a high diffusivity is applied to represent the through-layer crack, or is it necessary to also resolve the crack spatially and model sorption to its surfaces and tip? The first possibility is consistent with the approach currently applied in BISON, whereas the second possibility would indicate that the crack surfaces and/or tip have important influences on FP transport, potentially due to the temperature difference across the depth of the crack and its impact on equilibrium FP concentration at constant partial pressure. This was not meant to be an exhaustive analysis. Instead, it was intended to qualitatively assess the relative importance of the various physical behaviors to guide ongoing model development and future model application.

The assessment was conducted using a 2D version of the input developed for AGR-2 compact 2-2-3, discussed earlier in this chapter. The IPyC was completely removed from the lower half of the particle to represent an extreme form of IPyC damage. The resulting computational domain is shown in Figure 3.5. The upper hemisphere, midplane, and lower hemisphere of the particle represent idealized versions of the uncracked IPyC, surface of an IPyC crack, and tip of an IPyC crack, respectively. Mortar techniques were applied to model the:

- Mechanical contact between the buffer and the remaining IPyC
- Heat transfer from the buffer to the remaining IPyC in the upper hemisphere and the SiC in the lower hemisphere
- Sorption mass transfer from the buffer to the remaining IPyC in the upper hemisphere, from the buffer to the transition representing the crack surface at the midplane, and from the buffer to the SiC in the lower hemisphere.

IPyC sorption constants were applied to the surface of the SiC in the lower hemisphere to represent residual IPyC material. While overly simplified and far more extreme than typical IPyC damage, this modeling approach allows for quick and direct comparisons of transport behaviors in the presence of the various structural features.

The EOL temperature distribution and Cs concentration are also shown in Figure 3.5. The kernel and buffer, which are held stationary at the particle center, are cooler in the vicinity of the remaining IPyC where the gap is smaller and therefore impedes heat transfer less. Of the outer layers exposed to the gap, the inner surface of the IPyC is hottest, followed by the transition at the midplane and the inner surface of the SiC. The inner surfaces of the IPyC and SiC differ by about 1°C. The azimuthal uniformity of the EOL Cs concentration suggests that these structural and thermal differences do not significantly affect Cs transport. This observation is reinforced by the radial concentration data plotted in Figure 3.6, which were sampled from the upper particle centerline, the midplane, and the lower centerline.

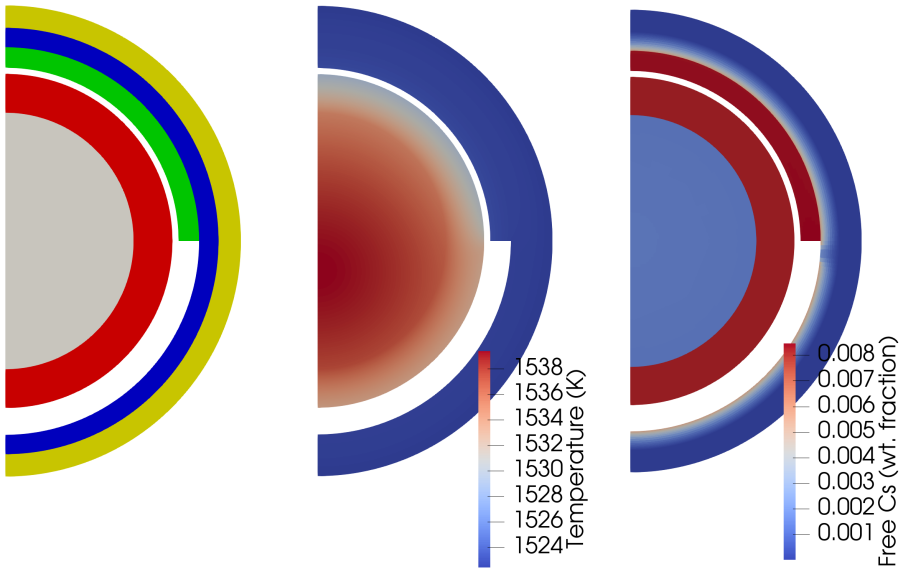

Figure 3.5. Results from a preliminary multiphysics study conducted to assess whether applying sorption mass transfer to spatially resolved crack surfaces has a significant impact on transport predictions. The figure shows the computational domain (left), EOL temperature (center), and EOL Cs concentration (right).

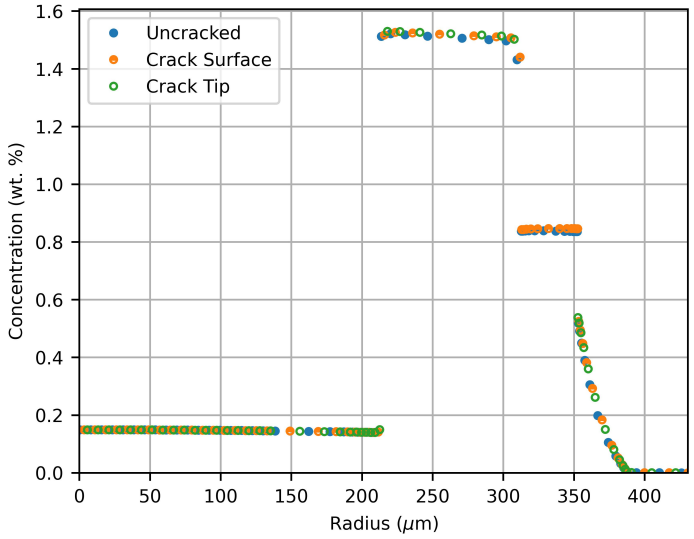

Figure 3.6. Comparison of radial Cs concentrations sampled from the regions of the particle that represent the uncracked IPyC, the crack surface, and the crack tip.

The data show that there is little difference between the three regions, which makes sense for several reasons. First, Cs melts at about 30°C and boils at about 670°C. The gap, having temperatures in excess of 1250°C, would therefore not be expected to provide an effective barrier for Cs transport. Similar behaviors would be expected from gaseous Kr and Xe. The gap may be more of an impediment to the transport of Ag and Sr, which have higher melting and boiling points. Second, while adsorption of Cs onto the outer layers (including the crack surfaces) depends on temperature, the 1°C difference between the surfaces does not appear to be enough to produce significant spatial heterogeneities. Finally, the intact SiC minimizes Cs transport out of the particle. This allows time for any azimuthal Cs gradients that may form inside the particle to homogenize.

Overall, the observed behaviors suggest that spatially resolving a crack and modeling sorption mass transfer to its surfaces and tip are unnecessary at this time. Smeared, nonretentive diffusivities should therefore be sufficient for representing the effects of layer cracks on FP transport. It should be noted that all FP diffusion within the TRISO particles is currently assumed to be isotropic. Potential differences between bulk and surface diffusion are also neglected. Unfortunately, the available data are not sufficient to refine the transport models at this time. The authors recommend reassessing the validity of the layer-cracking approximation if and when these behaviors can be better resolved.

Referring back to Table 3.2, partial and full layer debonding were adequately considered using contact methods under the assumption that interfaces are strengthless. Cohesive zone method and mortar-based debonding techniques are under development for modeling interfaces with nonzero strengths, but they are not considered in the current work. Sorption mass transfer models were applied to simultaneously model transport across bonded and debonded interfaces and answer the question: How do the magnitudes and characters of transport across each compare? Buffer–IPyC debonding was chosen for the assessment due to its prevalence in TRISO particles. As stated before, this was intended to be a qualitative rather than an exhaustive analysis.

As before, the assessment was conducted using a 2D version of the AGR-2 compact 2-2-3 input. The buffer-IPyC interface was debonded in the lower half of the particle and remained continuous in the upper half of the particle throughout the simulation. Mechanics and deformation were not modeled because doing so would have produced unrealistically high stresses at the static debonding tip and hindered convergence. Nevertheless, this setup allows for FP transport through the heterogeneous structure to be compared. The computational domain is shown in Figure 3.7. Mortar techniques were applied to model heat transfer and sorption mass transfer between the debonded buffer and IPyC in the lower hemisphere.

The EOL temperature distribution and Cs concentration are also shown in Figure 3.5. As expected, the temperature is continuous throughout the bonded upper hemisphere. It is discontinuous across the gap in the lower hemisphere, but the temperature drop across the gap is minor. There is significant azimuthal variation in the Cs concentration within the IPyC. Specifically, the Cs concentration is higher in the debonded region than in the bonded region. This result is less intuitive but also not surprising. On the one hand, mesh continuity in the upper hemisphere requires local continuity of both Cs concentration (in mol/m^3 or similar) and mass flux. On the other hand, sorption constraints in the lower hemisphere require surface concentrations that satisfy the equilibrium of partial pressure equality and the global preservation of mass flux. No azimuthal variations were observed in the previous simulation because sorption was applied throughout the particle, albeit at different gap distances and temperatures. Azimuthal variations are observable here because distinctly different physical processes—bulk diffusion versus sorption mass transfer—are being modeled

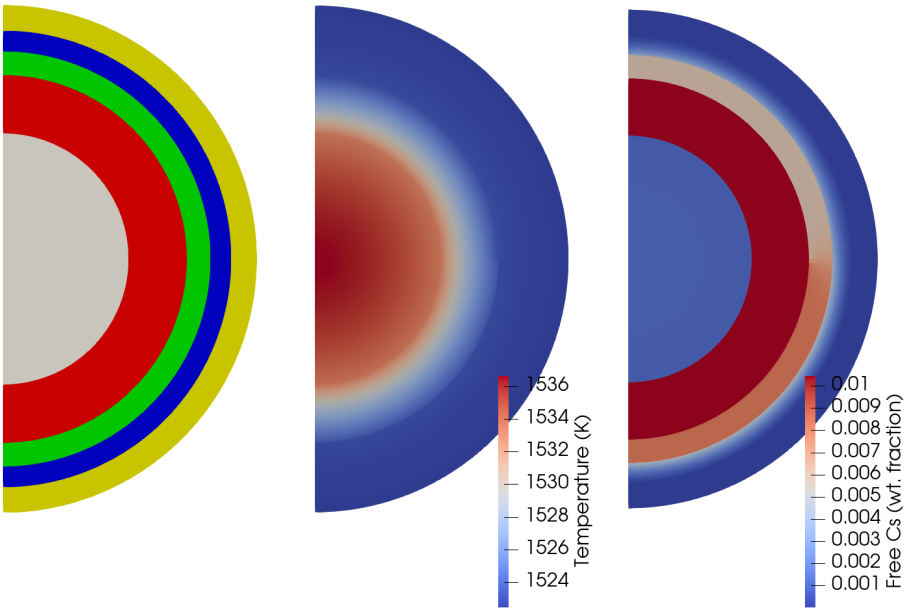

Figure 3.7. Results from a preliminary multiphysics study conducted to assess differences in the character and magnitude of FP transport through bonded and debonded interfaces. The figure shows the computational domain, where only the lower hemisphere is debonded (left), EOL temperature (center), and EOL Cs concentration (right).

in the two hemispheres.

As before, the retentiveness of the SiC allows time for the Cs concentration to begin to homogenize within the IPyC. This can be seen at the particle midplane, but not enough time has passed to completely eliminate the concentration gradient between the two hemispheres. Radial concentration data from the upper particle centerline, the midplane, and the lower centerline are plotted in Figure 3.6 to help visualize the differences between the regions. The results confirm that the IPyC Cs concentration is highest in the debonded region, lower in the transition region, and lowest in the bonded region. A similar trend can be observed in the SiC, which indicates that Cs migrates differently though gaps than through continuous solids and that debonding could affect Cs release even from intact particles.

While this is not a surprising behavior for Cs with its low melting and boiling points, it should be emphasized that the observation above is based on a limited set of purely computational results obtained from simulations that relied on diffusivities and sorption constants with significant uncertainties. It seems premature to draw more general or definite conclusions at this time. The authors recommend further study through additional particle-scale characterization and experiment validation using the methods laid out earlier in this chapter. Nevertheless, the current results show notable differences between transport through bonded and debonded interfaces, and that the behavioral models available in BISON are ready to be applied to study these behaviors.

The preliminary multiphysics studies presented in this section demonstrate the key BISON capabilities needed to

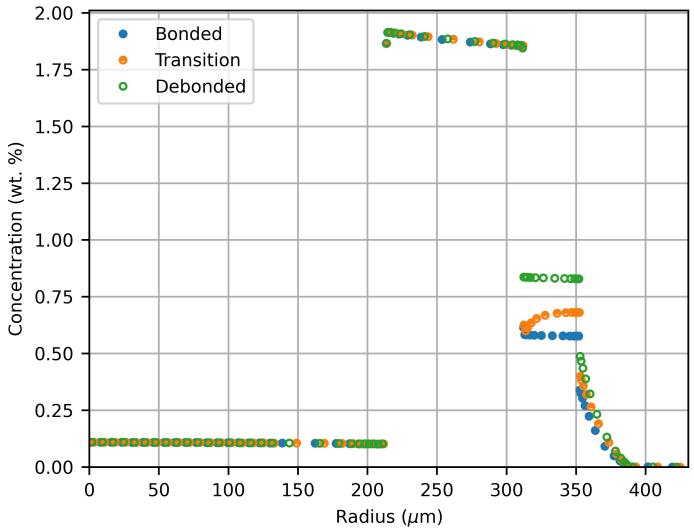

Figure 3.8. Comparison between radial Cs concentrations sampled from the bonded and debonded regions of the particle and the transition region between them.

model the effects of particle deformation and damage on FP transport and release. Preliminary results indicate that smeared, nonretentive diffusivities provide a suitable approximation for through-layer cracks and that the behavioral models available in BISON can be applied to study differences between transport across bonded and debonded interfaces. These results lay the groundwork for the refinement of thermomechanical damage and failure models in the next chapter and more in-depth multiphysics demonstrations in the following chapter.

3.4 Summary

Accurate radioactive nuclide release predictions for TRISO fuel systems require accurate models for intra- and interlayer FP transport within particles and accurate models for transport through the fuel element matrix. Until recently, it was assumed the interfaces between particle layers were continuous. Particle release predictions were scaled up to estimate compact-scale release and compared to results from integral effects irradiations. Shortcomings and challenges associated with this approach include oversimplification of the particle transport physics and the large uncertainties that arise from comparing particle-scale predictions to compact-scale experimental measurements. This work focused on improving particle-scale transport models and demonstrating a proof-of-concept approach to model validation at the particle scale.

Two behavioral model modifications motivated by particle-scale EPMA data were made to reproduce the observed behaviors. First, new buffer characterization data from the literature were used to calculate an appropriate surface density for the buffer–IPyC gap for use in the sorption mass transfer model. An initial buffer solid-phase density of 1,221 kg/m^3 was calculated from an initial overall buffer density of 1,050 kg/m^3 and initial porosity of 14%. Coupling to buffer densification and porosity evolution models in BISON predicted that porosity closed within the first 1%

FIMA burnup for the AGR-2 experiment, ultimately yielding a material with a density that is approximately 70% of its theoretical density. Applying this density correction in the sorption mass transfer model yielded reasonably accurate radial Cs concentration profiles when compared to the EPMA scans.

A preliminary model was then developed to simulate postulated FP trapping in the low-density buffer. The model was then calibrated to the experimental data, demonstrating satisfactory agreement with the EPMA scans when the potential barrier associated with escaping a trap is only 1% higher than the barrier associated with trapping. While trapping in the buffer remains hypothetical, including it as an option yields a flexible computational framework that delivers reasonable results when compared to the limited experimental data currently available. These new features establish a new pathway to model calibration and validation at the particle scale, which could potentially lower uncertainties relative to compact-scale validation efforts. Recommendations for follow-on experimental and modeling work focused on particle-scale validation were given.

Finally, preliminary multiphysics studies were conducted to assess the effects of different particle deformation and failure behaviors on FP transport and release. The studies confirmed that the use of smeared, nonretentive diffusivities provides a suitable approximation for through-layer cracks, motivating the development of a smeared cracking methodology that will provide a consistent thermomechanical and thermochemical modeling approach. The studies also demonstrated how the behavioral models available in BISON can be applied to study differences between transport across bonded and debonded interfaces, laying the groundwork for more in-depth multiphysics demonstrations. Future work in these areas may include:

- Collecting and assessing additional diffusivity and sorption isotherm data for key FPs and developing them into dedicated BISON classes rather than entering them in input files
- Performing additional particle-scale calibration and validation as more experimental data becomes available
- Undertaking more in-depth multiphysics analyses to characterize the spatial and dimensional effects of layer cracking and debonding on FP transport and release.

4. DAMAGE

As described in the previous chapter, FP transport is expected to be sensitive to the two main categories of particle damage: layer debonding and layer cracking or fracture. Existing debonding models can be readily coupled to FP transport models via sorption interface constraints. However, explicit fracture methods must be developed to simulate the realistic effects of localized layer fracture on FP transport. This chapter details the methodology developed to enable the simulation of explicit fracture using methods similar to those of the TRISO failure statistics models that were already developed and implemented in BISON.

4.1 Existing TRISO Failure Methods

BISON currently contains several categories of models and techniques that can be used to describe TRISO layer failure. These include discrete layer cracks, which are meshed *a priori* using the extended finite element method (XFEM); stress intensity factors, which account for crack geometry to accurately predict the effects of preexisting cracks on the stress states of surrounding materials; buffer–IPyC, IPyC–SiC, and SiC–OPyC interface debonding, which is described using cohesive zone modeling (CZM); and global failure probabilities calculations, which incorporate Weibull failure statistics and can be applied using Monte Carlo, direct integration, and variance reduction techniques. The content of this chapter focuses on layer cracking or fracture.

BISON currently uses statistical models to predict particle failure in response to given operating conditions and the stresses they produce [3]. Weibull distributions, which are fit to observed fracture stresses from numerous failure experiments, are used to define fracture criteria for individual TRISO particle layers. BISON-predicted stresses are then compared to these criteria to calculate failure probabilities, which should correspond to the failure probabilities observed in those experiments. A brief summary of these techniques is provided below. The cumulative Weibull distribution function P is given by:

$$P = 1 - \exp\left[-\left(\frac{\sigma_c}{\sigma_{ms}}\right)^m\right], \tag{4.1}$$

where σ_c is the maximum stress, σ_{ms} is the effective mean strength, and m is the Weibull modulus. The effective mean strength is further defined as:

$$\sigma_{ms} = \frac{\sigma_0}{I_n^{\frac{1}{m}}}, \tag{4.2}$$

where σ_0 is the characteristic strength, and I_n is the normalized stress distribution derived using the principle of inde-

pendent action. I_n is further defined as:

$$I_n = \frac{\int_V \left(\sigma_1^m + \sigma_2^m + \sigma_3^m\right) dV}{\sigma_c^m}, \tag{4.3}$$

where σ_c is now the maximum principal stress anywhere in the structure, σ_i are the tensile principal stresses, and V is the volume under consideration.

Currently, a Weibull distribution is sampled once for a given layer in a given particle and applied to define a single spatially uniform fracture criterion for that particle's entire lifetime. This approach assumes that the sampled fracture strength describes the resistance of the layer to fracture uniformly throughout its volume. The stress states throughout that layer are compared to that criterion at each time step to determine whether cracking occurs. When that criterion is met, a through-layer crack is assumed to form immediately. Additional simulations with discrete meshed cracks can then be leveraged to capture the effects of a crack in one layer to help determine the probability of cracking in adjacent layers. Such is the case when a crack forms in the previously-intact IPyC, which concentrates stress at the inner surface of the intact SiC, increasing the likelihood of SiC cracking. It is typically assumed that layers with cracks contribute very little to FP retention regardless of crack geometry or where the crack occurs spatially.

Stress intensity factor modeling capabilities were recently developed to help refine this approach [10]. In order to calculate the stress intensity factor, an interaction integral is evaluated for the area around the tip of a meshed crack. The geometry of the area around the crack tip must be accounted for in the integral. If the calculated stress intensity factor exceeds the fracture toughness of the material, the crack is assumed to propagate. This method works particularly well for functionally graded materials and may be applied in future analyses to study the transition in properties between TRISO layers. Its use can enhance the accuracy of BISON predictions by helping to determine whether or not a crack will propagate through a layer (as opposed to immediately inducing through-layer fracture in all cases), but it does not help identify where in the layer a crack may form or how it might propagate spatially. These aspects of cracking may be important because cracks are frequently observed in the vicinity of debonded interfaces and other cracks.

Because the methods discussed above require prescribed cracks, they cannot be applied to study realistic cascading multiphysics failure mechanisms. The current work aims to incorporate aspects of the above techniques and account for spatial variations in material strength to simulate statistical fracture locally within the SiC layer. Rather than sampling a Weibull strength distribution once for the entire layer, in this approach a distribution is sampled multiple times to define spatially varying fracture criteria on a per-element basis. These spatially varying fracture criteria can then be compared to spatially varying stress states within the material to predict local crack formation and propagation, or lack thereof. The predicted failure behaviors should be similar to those obtained using the previous technique at the particle layer scale, but this method will additionally allow for the simulation of local FP transport in response to local cracking. The details associated with the development of this new methodology are described in the sections below.

4.2 Smeared Cracking

A *smeared cracking* method was previously implemented in MOOSE so that fracture within a finite element mesh could be simulated without the need for meshing the cracks themselves [29]. It has been applied previously to simulate

fracture in other fuel types with promising results [30]. The method reduces the local elastic properties of a material to represent the formation of a crack when the local stress state exceeds a local material limit. Cracks are therefore free to form naturally throughout the material in response to local variations in stress and strength. A fine mesh is required with this method to accurately capture the mechanical effects of a crack on the stress state of the surrounding material. Smeared cracking is otherwise ideal for the current work because (1) it can be applied to study realistic fracture behaviors by supplying the model with spatially varying strengths sampled from Weibull distributions, and (2) it can be coupled directly to diffusion models to capture the effects of cracking on FP transport and eventual release.

The development of this new methodology and its application to the SiC layer is separated into three steps that are detailed in the following sections: (1) developing methods for seeding per-element fracture strengths across the mesh using Weibull statistics; (2) comparing BISON predictions to results obtained from hemispherical SiC shell crush tests to confirm consistency with experimental failure observations, adjusting the Weibull distributions as necessary; and (3) incorporating the smeared cracking model with a sampling technique that accounts for material volume and mesh density.

4.3 Initial Mesh Seeding

In order to account for statistical spatial variations in the fracture strength, a new sampling method was incorporated into the SiC fracture model. The new model samples from a Weibull distribution at each quadrature point in the mesh. Figure 4.1 shows the initial Weibull probability density function used to seed the fracture strengths for the SiC mesh. Recall that this is not the same probability density function that was derived from observed fracture stresses of macroscopic specimens. Instead, it is a distribution of the fracture strengths of individual elements within those specimens that, when simulating those failure experiments, generates comparable failure statistics. Figure 4.2 shows the cumulative probability of encountering increasing fracture strengths.

The distributions mentioned above were sampled to seed per-element fracture strengths for a 2D axisymmetric mesh representing a hemispherical SiC shell. Example results are shown in Figure 4.3. The results show how the fracture strength varies spatially throughout the mesh. In contrast with the existing Weibull sampling technique, in which the strength of the entire layer is defined by a single value based on observed failure statistics, this technique increases the spatial resolution of damage predictions by allowing fracture strengths and the microstructural flaws that they represent to vary spatially within the mesh. For a given stress, some elements are more likely to fracture than others. Cracks that initiate in elements surrounded by low-strength elements would be more likely to propagate than those that initiate in elements surrounded by high-strength elements. Both techniques should produce similar predictions in terms of whether a given sample is expected to completely fail due to cracking, but the new technique offers the opportunity to study how cracks form and propagate to induce failure.

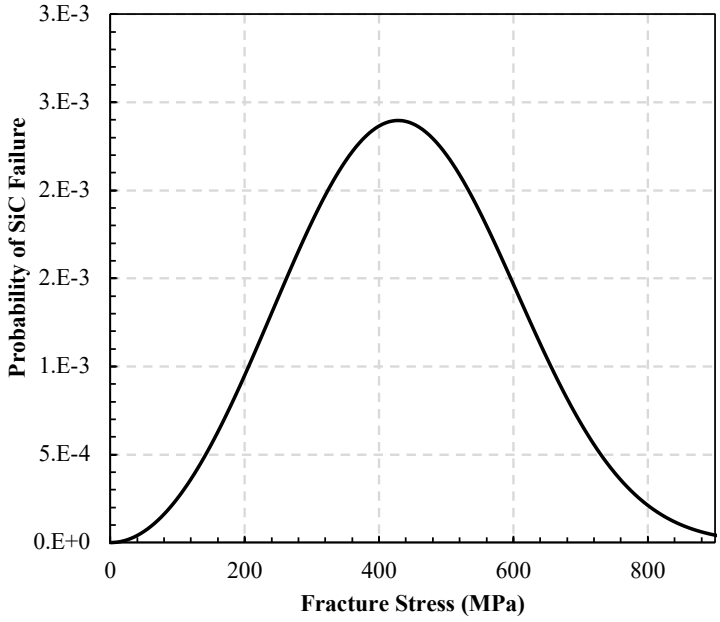

Figure 4.1. Weibull distribution describing the probability of sampling different SiC fracture strengths. This distribution can be sampled randomly on a per-element basis to seed a SiC mesh with spatially varying strengths representing a spatial distribution of microstructural flaws.

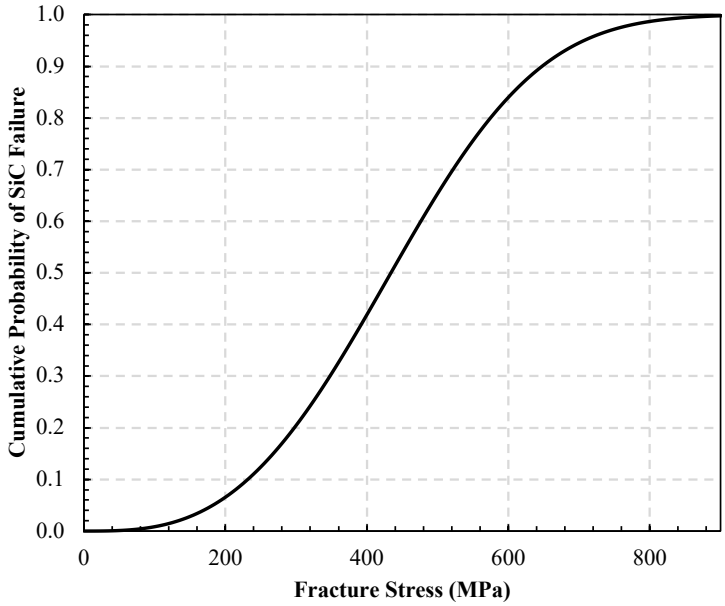

Figure 4.2. Cumulative probability of sampling increasing fracture strengths.

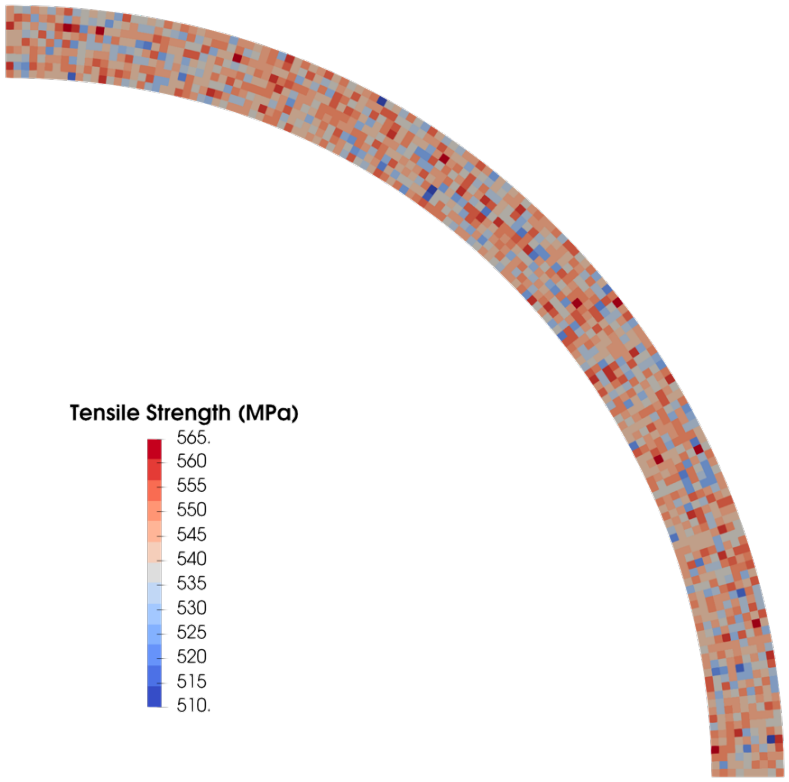

Figure 4.3. Results obtained from seeding per-element fracture strengths for a 2D axisymmetric mesh representing a hemispherical SiC shell.

4.4 Experimental Comparison

In order to ensure that the SiC fracture strength distribution would produce realistic failure probabilities, simulations were run for comparison with a subset of the experimental measurements from which the original distributions were derived. The experiments used for this comparison, which were conducted at Oak Ridge National Laboratory (ORNL), involved crushing hemispherical SiC shells in a mechanical press [31]. The SiC was fabricated using a process and had structures and properties similar to that used in the AGR-1 experiment. Figure 4.4 illustrates the BISON simulation setup of these crush tests and the original experimental diagram. The setup included top and bottom rams with a piece of brass foil and a SiC shell in between. The brass foil was intended to deform to more evenly distribute the force from the top ram onto the top of the shell. The top ram was loaded until the shell was crushed. The BISON simulation results in the figure show that high tensile stresses formed at the inner shell surface below the brass foil and just beyond the foil. This is consistent with the experimental observation that shell failure occurs at the midheight of the hemisphere.

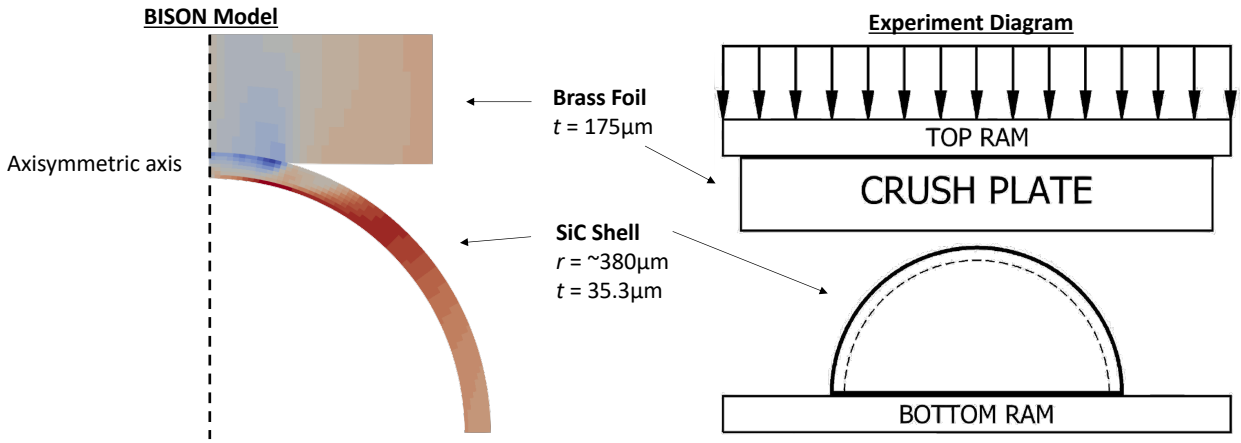

Figure 4.4. Example of a hemispherical crush test conducted using a 2D axisymmetric model in BISON (left) and a diagram, reproduced from Reference [31], of the experimental setup of the crush tests (right). The top and bottom rams were modeled using boundary conditions in the simulations.

In order to interpret the data from the experimental crush tests, analytical formulas for this loading scenario were used to determine the peak stress in the shell [32, 31]. The peak stress σ_{max} accounts for two contributions and is given by:

$$\sigma_{max} = \sigma_{membrane} + \sigma_{bending}, \tag{4.4}$$

where $\sigma_{membrane}$ is the membrane stress, and $\sigma_{bending}$ is the bending stress. The two contributions are further defined as:

$$\sigma_{membrane} = C_1 \frac{F\sqrt{1-\nu^2}}{t^2}, \tag{4.5}$$

$$\sigma_{bending} = -C_2 \frac{F(1+\nu)}{t^2}, \tag{4.6}$$

where F is the load in N, ν is Poisson's ratio, t is the shell thickness in meters, and C_1 and C_2 are unitless fitting

parameters.

The fitting parameters, which account for sample geometry and deformation during loading, are further defined as:

$$C_1 = 0.2205 - 0.04\mu - 0.0115\mu^2, \tag{4.7}$$

$$C_2 = 1.2044 \exp\left(-1.2703\mu\right). \tag{4.8}$$

Finally, the parameter μ is further defined as:

$$\mu = r_o \left[\frac{12\left(1-\nu^2\right)}{R_2^2 t^2} \right]^{\frac{1}{4}}, \tag{4.9}$$

where r_o is the radius of the area of contact in meters, and R_2 is the average radius of the hemispherical shell in meters. The parameters used in the equations above are illustrated in Figure 4.5.

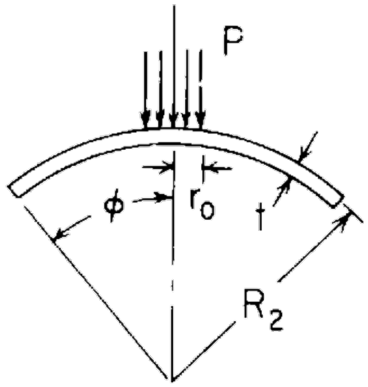

Figure 4.5. Diagram for the calculation of the peak stresses in the hemispherical crush tests, where P is the pressure, ϕ is the angle of the hemisphere, r_0 is the radius of the area of contact, t is the shell thickness, and R_2 is the average radius. Reproduced from Reference [32].

The crush tests were simulated in BISON using a brass foil thickness of 175 μm, a SiC shell radius of 380 μm, and a SiC shell thickness of 35.3 μm. This experimental series was designed to reflect the SiC layers in the AGR-1 TRISO particles. Figure 4.6 shows a comparison of the simulated and experimental crush test results in terms of peak principal stress versus applied load. This comparison shows good agreement between the peak stresses reported by the BISON model (red line) and the experimental measurements (blue markers), which were interpreted using the equations above [33]. The scatter in the experimental results is believed to arise from asphericity and nonuniformities in the geometries of the SiC shells. BISON simulations are capable of accounting for these features, but they were excluded from these simulations because the individual shells were not characterized to that level of detail.

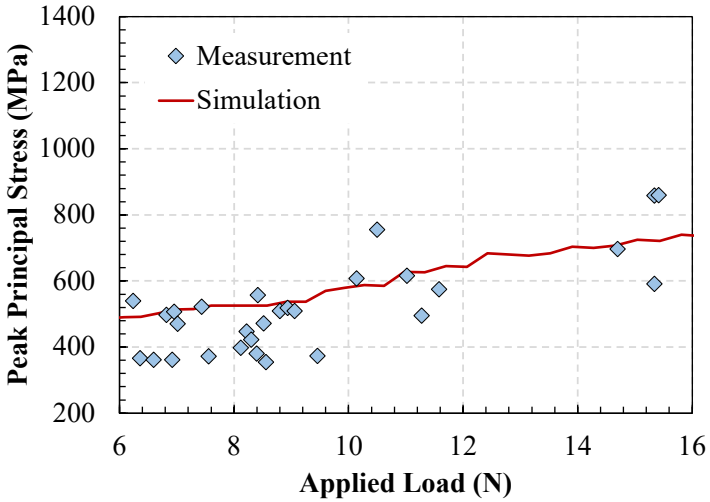

Figure 4.6. Peak principal stress versus applied load in the SiC shells for an AGR-1 data series (blue markers) [33] and calculated using the BISON crush test model (red line).

4.5 Refined Mesh Seeding

During the course of this work, the impacts of element volume and mesh density were investigated. In particular, the method used to sample from the Weibull distribution and seed fracture strengths across the mesh was modified to account for these features. Generally, the propensity of a brittle material to fracture in response to a given stress increases with increasing specimen size due to the probability of a critical flaw being present in that volume. This means that, at least for this analysis, the fracture strength of a SiC shell should decrease for larger shells.

Prior work compared the global failure probability of SiC specimens based on their fracture strength for internally pressurized tubes and hemispherical crush tests [34]. Figure 4.7 shows a comparison of these two types of failure testing. The internally pressurized tubes are much larger than the SiC hemispheres and thus possess an overall lower fracture strength. Note that the data are plotted on logarithmic axes. This highlights the significance of the impacts of sample volume and material type on failure probability at a given fracture strength.

The fracture strengths of individual elements should depend on their size in a similar manner. Larger elements represent larger volumes of material, which are more likely to contain critical flaws than smaller elements. This observation is particularly important because the volumes represented by elements in 2D axisymmetric meshes (and 1D spherical meshes) vary with their position relative to the axis (or point) of symmetry. This effect was accounted for by weighting the fracture strengths sampled from the Weibull distribution using:

$$\frac{\sigma_{mf,1}}{\sigma_{mf,2}} = \left(\frac{V_2}{V_1}\right)^{\frac{1}{m}}, \tag{4.10}$$

where $\sigma_{mf,1}$ is the reference strength in Pa, $\sigma_{mf,2}$ is the element strength in Pa, V_1 is the reference sample volume in m^3,

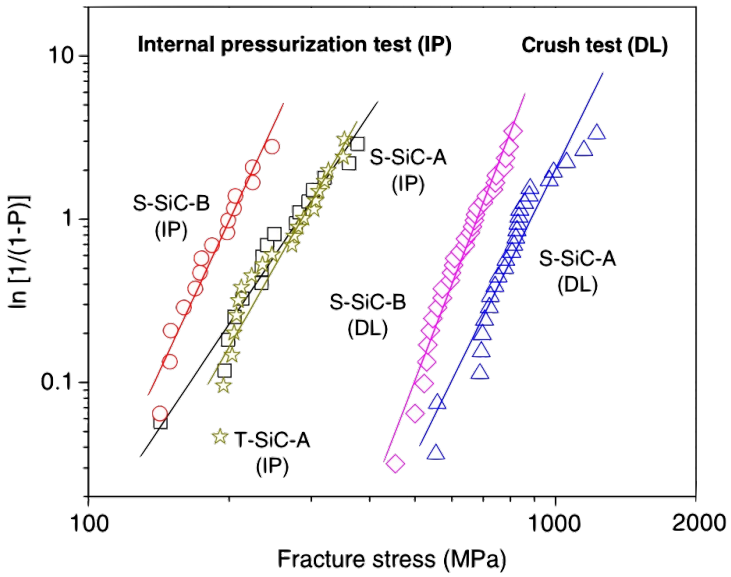

Figure 4.7. The fracture strengths of SiC samples depend strongly on their size due to the likelihood of a sample containing a critical flaw in the material. The fracture stress is larger for smaller samples (crush tests) than for larger samples (internal pressurization tests). Reproduced from Reference [34].

and V_2 is the element volume in m^3. This allows the sampling algorithm to correctly seed the mesh based on individual element volumes.

Fracture strengths seeded for a hemispherical SiC shell using the element volume correction are shown in Figure 4.8. Because the shell is represented using an axisymmetric coordinate system, the elements actually represent rings when rotated about the axis of symmetry. Elements closer to the axis (those near the top of the shell) have smaller volumes, are less likely to include critical flaws, and therefore have larger fracture strengths. Conversely, elements farther from the axis (those near the bottom of the shell) have larger volumes, are more likely to include critical flaws, and therefore have smaller fracture strengths. Similar arguments could be applied to spherical 1D meshes where each element represents a spherical shell, the volumes of which increase with distance from the origin. Fracture strengths seeded for 3D Cartesian meshes, on the other hand, would require significantly less volume-weighting.

The volume correction above accounts for the change in the likelihood that a region of interest includes a critical flaw when moving from one sample to another. Specifically, it is leveraged in the current work to transform the fracture strengths obtained from experiment specimens to those needed to represent a single element in a simulation while accounting for differences in element volume in the process. However, the volume correction does not account for the influence of mesh density on the sampled distribution. Consider two simulations that have the same domain (i.e., sample volume) but drastically different mesh densities. The simulation with the low mesh density would be seeded with a small number of samples that likely cluster around the distribution mean. In contrast, the simulation with the high mesh density would be seeded with a large number of samples and would therefore be more likely to include fracture strengths that are significantly less than and significantly greater than the mean. The simulation with the high

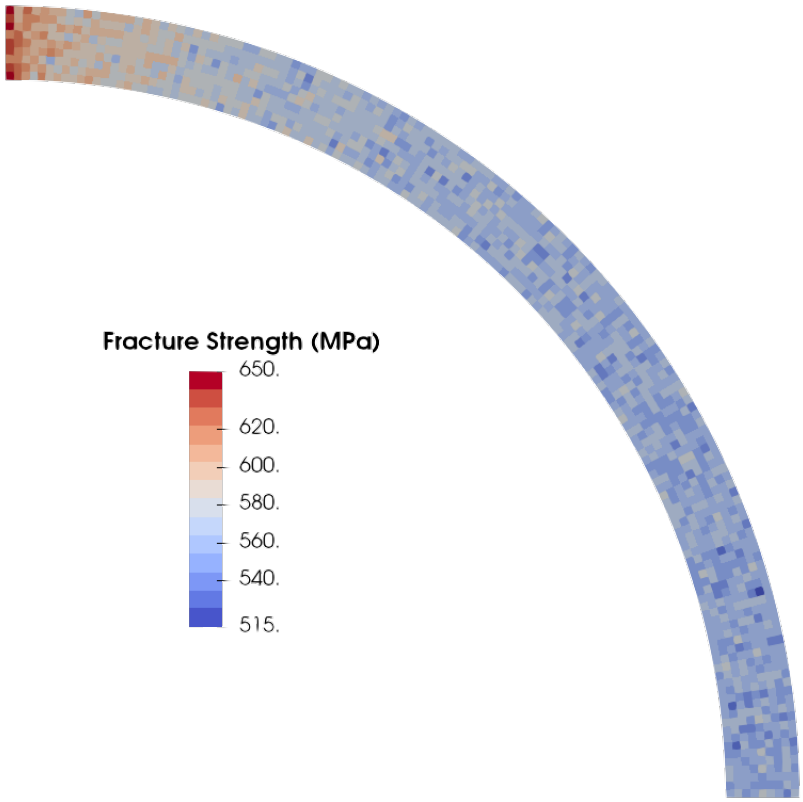

Figure 4.8. An example of mesh seeding after volume-weighting is applied to each element. Due to the axisymmetric assumption in this geometry, elements farther from the axis of symmetry have much larger volumes, are more likely to contain critical flaws, and therefore have lower fracture strengths.

mesh density would be more likely to fail at a lower applied stress than the simulation with the low mesh density.

Ideally, simulations representing the same domain but having different mesh densities should yield consistent failure behaviors to the extent permitted by the nature of the random sampling method. Methods for enforcing this behavior are under investigation. One potential solution involves truncating the upper end of the distribution as the fraction of the total volume represented by each element increases, as show in Figure 4.9. Another potential solution involves skewing the distribution toward lower values as a function of the same metric by changing the characteristic stress or distribution average. The authors recommend investigating these possibilities in future work.

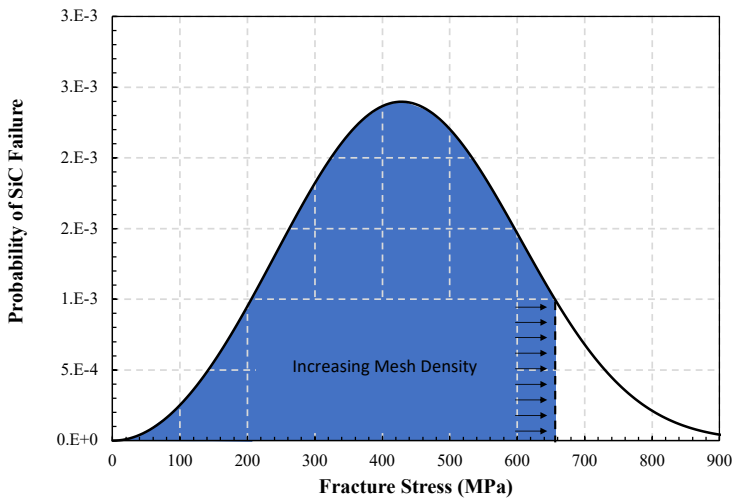

Figure 4.9. Potential method for enforcing the consistency of failure predictions for simulations having the same domain but different mesh densities. The upper portion of the Weibull distribution could be truncated according to a function based on the fraction of the total volume represented by each element. The authors recommend investigating these possibilities in future work.

4.6 Summary

This work describes progress that has been made toward applying a smeared cracking approach to simulate the statistical, spatially resolved fracture of the SiC layer within TRISO particles to enable the study of the effects of fracture on FP transport. A methodology was developed to incorporate the statistical nature of fracture strength into finite element simulations and validate this model using experimental measurements from hemispherical SiC crush tests. The next steps in this process involve developing a correction for mesh density and calibrating Weibull distribution terms to deliver failure probabilities that are consistent with the crush tests and other available experimental datasets. Additionally, future work should include the application of 3D simulations to confirm the behaviors and trends observed in the 2D results presented in this work. Longer-term research will focus on applying these techniques to other TRISO layers and coupling the smeared cracking models to FP transport models to enable the study of the cascading multiphysics failure behaviors observed in experiments.

5. MULTIPHYSICS

In Section 3, we discussed how smeared, nonretentive diffusivities provide suitable approximations for modeling the thermochemical effects of through-layer cracks. In Section 4, we began to develop a failure statistics-informed, mesh-independent methodology for applying smeared cracking to the SiC layer of TRISO particles, which can ultimately be extended to additional TRISO layers. Together, these capabilities will provide a consistent analysis framework that can be applied to study the tightly coupled thermomechanical and thermochemical behaviors associated with cascading particle failure behaviors. In this chapter, we model a variety of artificially damaged particles using the smeared diffusivity approach to (1) assess the validity of failure-related assumptions and simplifications frequently used in BISON, (2) make scientific observations to guide further research and model development, and (3) offer preliminary recommendations for how these models could be applied to support ongoing efforts to deploy TRISO-based fuels for commercial applications.

Within this context, FPs generally fall into two categories: reactive and nonreactive. Reactive FPs affect the structure, properties, and performance of the fuel form itself—potentially *contributing directly to* particle failure. Examples of reactive FPs include Pd and Ag, both of which participate in Pd penetration and associated failures. Nonreactive FPs don't affect the fuel form itself but are simply produced within it and are transported through it. These FPs *are sensitive to* particle failure in that it affects their release. Note that some FPs can be considered to belong to both categories. A hierarchy summarizing these behaviors is shown in Figure 5.1. In addition to presenting the types of FPs, the diagram identifies several important aspects of through-layer cracking behavior, including mesh density, problem dimensionality, crack formation and propagation, and crack diffusivity, and the modeling thereof. These topics form the basis of the specific multiphysics analyses discussed in this chapter.

Pd was selected for examination in this chapter. In addition to the aspects of through-layer cracking behavior identified above, preliminary mesoscale studies suggest that the microstructure that forms due to Pd penetration may depend on local reactant fluxes, which may in turn be affected by IPyC cracking and/or debonding. An initial investigation into the flux-concentrating effects of IPyC cracking is presented in Section 5.1. We then assess the importance of modeling crack propagation for release calculations and evaluate various ways of representing three-layer failures in Section 5.2 and Section 5.3. Studies focused on the effects of smeared crack size, diffusivity, dimensional effects, and timing are presented in Section 5.4 through Section 5.7. Finally, the findings of these analyses and recommendations for future work are summarized in Section 5.8.

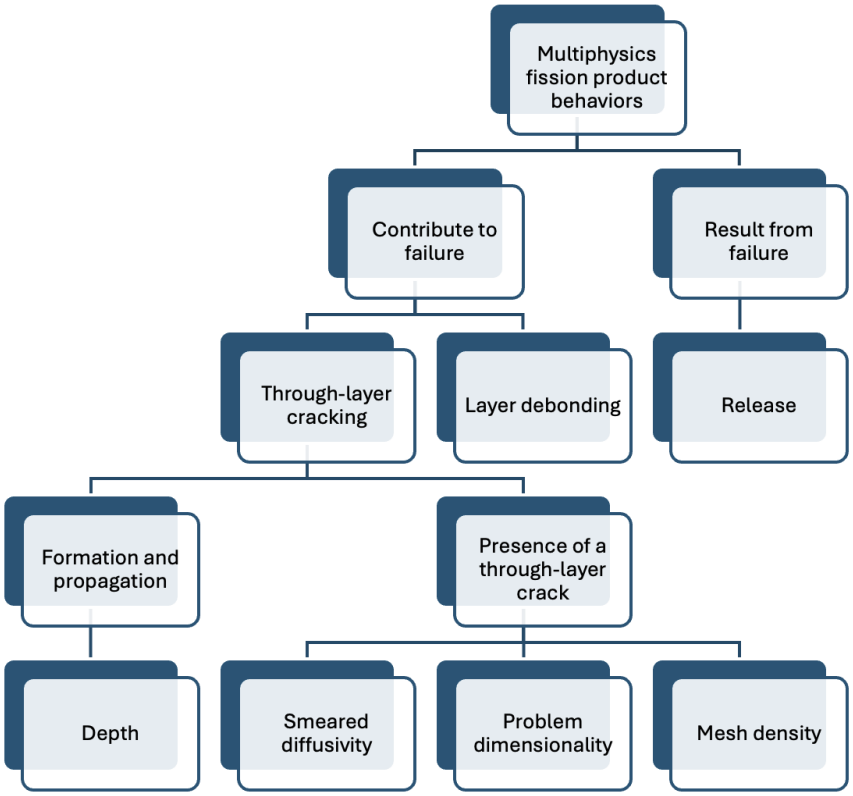

Figure 5.1. Overview of a subset of tightly coupled thermomechanical and thermochemical behaviors in TRISO particles and outline of the preliminary multiphysics analyses discussed in this chapter.

5.1 Flux Heterogeneity

As mentioned above, preliminary results from mesoscale studies conducted at INL indicate that the Pd penetration microstructure may be sensitive to heterogeneities in reactant flux at the inner surface of the SiC. Such heterogeneities could result from a crack in the IPyC. Pd would continue to migrate through the intact portions of the IPyC at or near its normal rate, while the crack could provide a high-diffusivity pathway for accelerated Pd transport to the SiC surface. The Pd flux through the crack would be expected to exceed the average flux across the IPyC–SiC interface. A simulation was constructed to begin to investigate and quantify this behavior to inform further LLS model development.

All results presented in this chapter were obtained using the nominal particle design given in Table 2.1 and transport parameters given in Table 2.4. The simulations used a particle surface temperature of 1300 K, constant power density of 2.03 GW/m^3, and EOL burnup of 20% FIMA. Particle mechanics and sorption mass transfer were omitted from the simulations to isolate the effects of various types of smeared cracks on Pd transport. The simulation presented in this section was conducted in 3D using quarter-particle symmetry and a mesh density typical for practical engineering applications.

A smeared, nonretentive diffusivity was applied to a small portion of the IPyC to represent a through-layer crack. The crack was assumed to originate during particle fabrication and was therefore present throughout the entire simulated particle irradiation. The 3D computational domain, crack setup, and EOL Pd distribution within the particle are shown in Figure 5.2. Red indicates the presence of a crack in the center image, and the kernel has been hidden to emphasize small variations in Pd concentration in the image on the right.

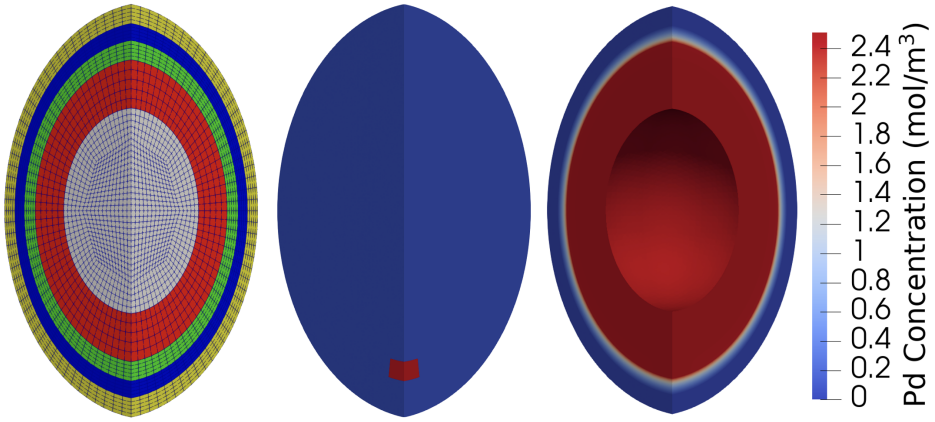

Figure 5.2. 3D TRISO particle domain used for multiphysics smeared diffusivity analyses (left); artificially damaged IPyC, where red indicates the presence of a crack (center); and the EOL Pd distribution within the particle, where the kernel has been hidden to emphasize variations in Pd concentration in the other layers (right).

The Pd distribution shown in the figure lacks noticeable heterogeneity due to the intact SiC and the IPyC's limited contribution to Pd retention. Two additional cases were run for comparison. The first featured a fully intact IPyC, and the second applied the commonly used *fully failed layer* approximation to the IPyC. The fully failed layer approximation involves homogeneously applying a smeared, nonretentive diffusivity to the entire damaged layer. The approximation is believed to be conservative and is computationally efficient because it is compatible with 3D, axisymmetric 2D, and spherical 1D analyses, but it lacks the ability to resolve transport heterogeneities that may form in the vicinity of a spatially resolved crack.

Average Pd fluxes were calculated at the inner IPyC surface for all three cases, and an additional sideset was used to sample the local flux through the crack area. The results, plotted in Figure 5.3, show that the average fluxes are about the same for the three cases. The flux through the crack area is significantly higher, approaching a value of 1.5–2 times that of the average flux at EOL. Nevertheless, the average flux sampled from the case with the spatially resolved crack is not significantly higher than that of the other cases due to the small ratio of crack surface area to total inner IPyC surface area. Comparing the predicted Pd releases for the three cases showed no significant variations, again emphasizing how limited the IPyC's contribution is to Pd retention.

This simple demonstration yields several important observations. If cracks provide high-diffusivity pathways for accelerated transport, then they will concentrate the flux of FPs in local regions of the particle. If the rate of Pd penetration is sensitive to the amount and heterogeneity of the reactant fluxes, as preliminary mesoscale results suggest, then these flux concentrations could elevate SiC degradation in those regions and the overall probability of particle

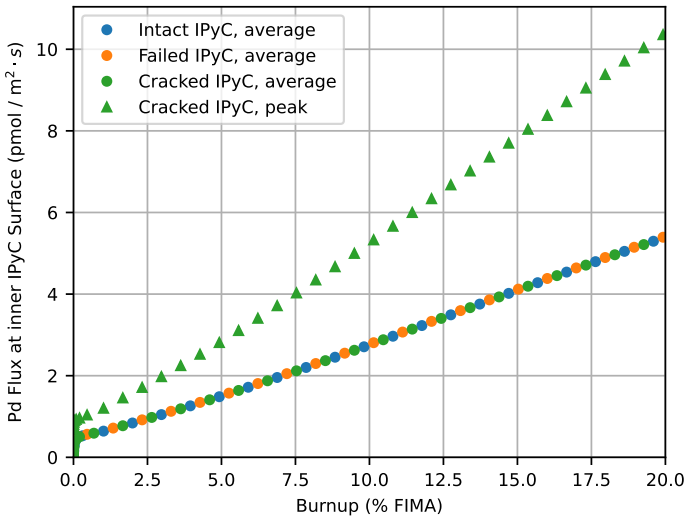

Figure 5.3. Average Pd fluxes at the inner surface of the IPyC obtained from three different cases, and peak flux from the case with the spatially resolved IPyC crack.

failure. As such, the fully failed layer approximation may not be completely conservative because it smears the flux of reactive FPs—and therefore Pd penetration depth—over the full inner surface area of the SiC. Its use may result in the underprediction of particle failure probability due to Pd penetration.

These flux-concentrating effects can only be captured by modeling a spatially resolved crack. Unfortunately, this is computationally demanding and completely incompatible with 1D simulations, which are all but required for practical particle failure analyses. However, it may be possible to capture the effects of reactant flux concentration on Pd penetration using a factor derived from the ratio of the average reactant flux to the reactant flux passing through the crack. This factor could be applied in conjunction with the fully failed layer approximation to capture the elevated rate of Pd penetration and its influence on failure probability when an IPyC crack is present. This could be done even when the crack hasn't been resolved.

The analysis in this section suggests that a factor of 1.5–2 would be appropriate, but this value is likely influenced by particle geometry, crack geometry, operating history, and more. LLS calculations using realistic crack dimensions may provide a more useful, generally applicable value. In the meantime, subsequent analyses presented in this chapter were extended to investigate the potential impacts of various parameters on flux concentration at the engineering scale to provide input for best practices when applying these rapidly evolving models.

5.2 Crack Propagation

Practical analyses involving the effects of particle damage on FP release are typically conducted under the assumption that the crack is either present or not (i.e., crack formation and propagation are neglected). The 3D model introduced in the previous section was applied to confirm the validity of this assumption. SiC cracks and/or IPyC–SiC debonding

are often observed in the vicinity of IPyC cracks due to the influence of the IPyC crack on its own local stress state and that of the SiC. Starting with the case with the spatially resolved crack from the previous section, the crack was artificially propagated through the SiC one element at a time to assess its impact on Pd release. Figure 5.4 shows a comparison of these simulations and two idealized cases: one with a fully failed IPyC and an intact SiC, and another with fully failed IPyC and SiC layers.

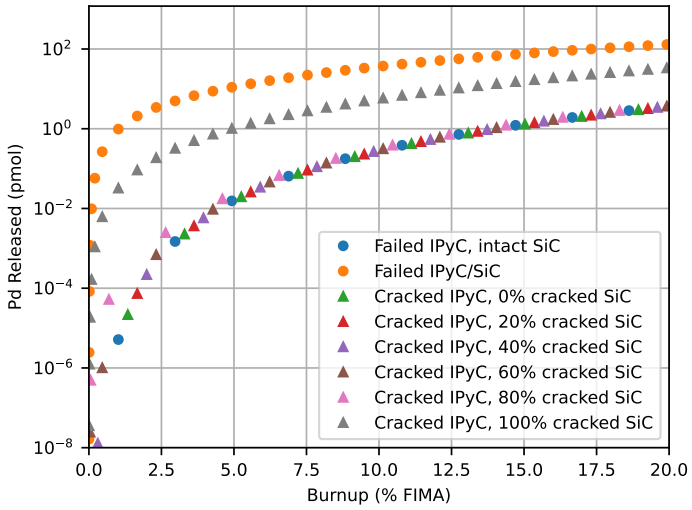

Figure 5.4. Pd release predicted for various spatially resolved SiC crack depths compared to two idealized cases.

The results show that BISON predicts nonzero Pd release, even for the case with the intact SiC. Pd release from the case with the fully failed SiC is predicted to be more than an order of magnitude greater. The releases predicted for the propagating spatially resolved crack are consistent with that of the intact SiC case until the crack completely penetrates the SiC. Release then increases dramatically and approaches, but does not reach, that of the fully failed SiC case. These results indicate that the fully failed layer approximation is conservative from a general FP release perspective, but care should be taken to balance conservatism with realism, particularly for calculations that may impact operating limits. Crack propagation through brittle ceramic materials like SiC is expected to be fast compared to particle lifetime, so neglecting crack formation and propagation appears to be justified. Focus should instead be placed on how to best represent through-layer cracks once they have formed.

5.3 Three-Layer Failures

The results presented in the previous section indicate that the intact OPyC provides a small amount of Pd retention, at least for the case with the spatially resolved crack. In this section, we extend damage to the OPyC to assess Pd release from TRISO particles for which all three retentive layers have been compromised. Again using the 3D model, we compare a spatially resolved three-layer crack to two idealized cases: one with a fully failed IPyC, fully failed SiC, and intact OPyC, and another with fully failed IPyC, SiC, and OPyC layers. Pd release predictions for the three

cases are shown in Figure 5.5. The results confirm that the OPyC's contribution to Pd retention is small. Predicted releases from the spatially resolved crack and fully failed cases are nearly identical, suggesting that the fully failed layer approximation is appropriate for completely compromised particles.

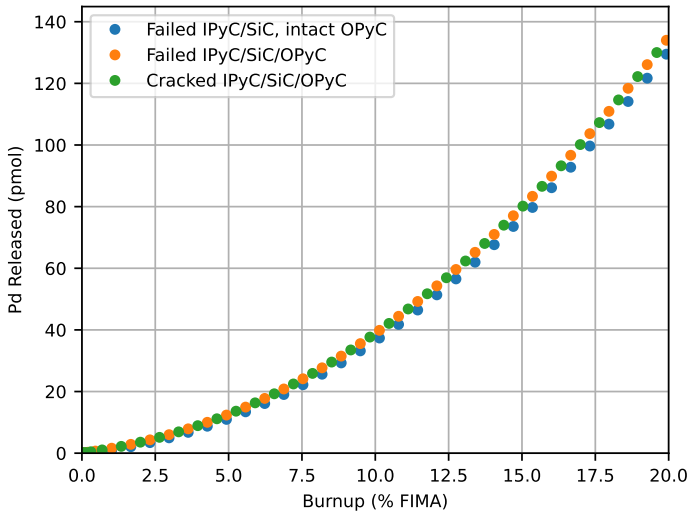

Figure 5.5. Pd release predicted for a spatially resolved three-layer crack compared to two idealized cases.

The Pd contents retained in various particle layers or released from the particle are plotted for the spatially resolved crack case in Figure 5.6. The results show that the overwhelming majority of Pd is retained within the kernel, which is consistent with the discussions in Section 2.4 for a particle surface temperature of 1300 K. Almost all Pd that migrates out of the kernel is released from the particle with almost all of that being released through the crack. Comparatively little Pd is retained within the other layers.

These observations indicate that Pd release is limited by both the kernel and the retentive layers while they remain intact. Even when all three retentive layers fail, the kernel itself presents a significant barrier to Pd transport and release. The same behavior would be expected for any FP for which the kernel diffusivity is not significantly larger than the diffusivities in the retentive layers. These observations highlight the importance of using complete sets of accurate source terms and layer diffusivities for each FP of interest.

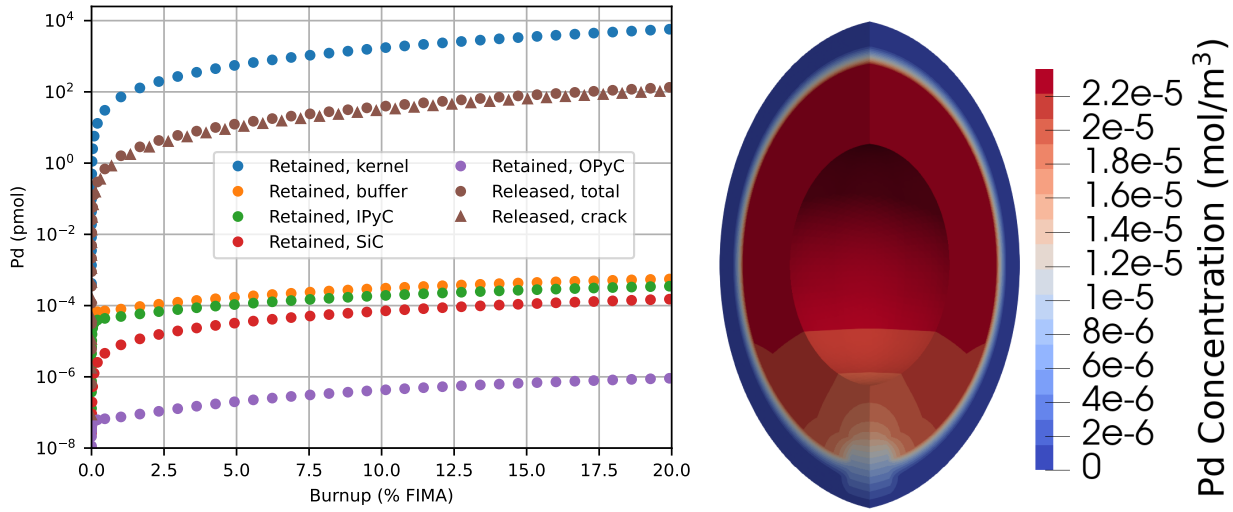

Figure 5.6. Pd contents retained in various layers or released from the particle for the spatially resolved three-layer crack case (left) and the EOL Pd distribution within the particle, where the kernel has been hidden and a discretized color scale has been used to emphasize variations in Pd concentration in the other layers (right).

5.4 Crack Size

The 3D model with the spatially resolved three-layer crack was then used to investigate the impact of smeared crack size on Pd release and flux predictions. Two additional cases were run with the crack side length halved and doubled. The Pd release predictions were nearly identical for the three cases, indicating that any reasonably sized crack simulated with a practical-engineering-scale mesh is sufficient to release nearly all Pd that escapes from the kernel. Average Pd fluxes at the inner IPyC surfaces and local fluxes through the crack areas are compared for the three cases in Figure 5.7.

The results show that the average Pd fluxes are identical for the three cases. Compared to the flux through the reference crack (orange), flux is lower through the larger crack and higher through the smaller crack. Flux is inversely proportional to smeared crack area, as expected, but this finding is not especially useful in terms of defining a reactant flux-concentration factor for Pd penetration modeling. This observation highlights the need for LLS calculations using realistic crack dimensions. Additionally, atomistic calculations could be used to calculate surface diffusivities for solid and liquid FPs. High, nonretentive values could likely still be used for gaseous FPs. It may then be possible to scale down a given diffusivity as the crack area is scaled up to a size that can be resolved at the engineering scale, preserving the overall throughput of the crack. With sufficient data, this approach could prove to be more accurate than existing methods. Regardless, the authors recommend validating predictions against FP retention data from failed particles as soon as possible.

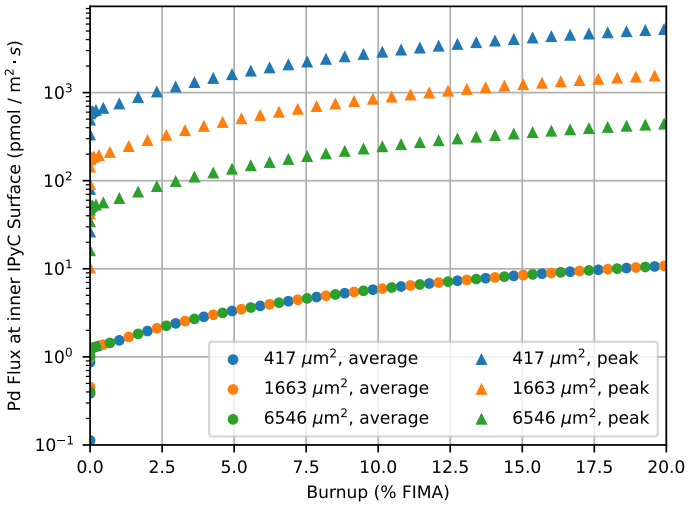

Figure 5.7. Average Pd fluxes at the inner IPyC surfaces and local fluxes through the crack areas for three spatially resolved three-layer cracks of different sizes.

5.5 Crack Diffusivity

In the absence of more realistic crack surface diffusivities, simulations were run to identify a suitable placeholder for use with the smeared cracking approach. Four additional cases were run using the 3D model and various smeared crack diffusivities. The results (presented in Section 5.3) used a diffusivity of 1×10^{-8} m^2/s and are compared to those of the four new cases in Figure 5.8. The results suggest that any diffusivity above 1×10^{-12} m^2/s is sufficient to release nearly all the Pd that escapes from the kernel. The authors recommend selecting values that balance conservatism and computational expense until more realistic values can be defined.

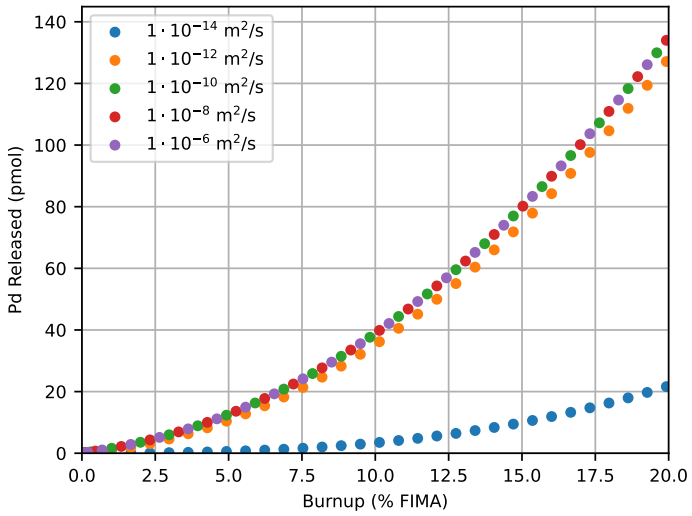

Figure 5.8. Pd release predictions obtained using various smeared crack diffusivities.

5.6 Dimensional Effects

3D TRISO particle simulations offer the highest possible fidelity because they do not inherently assume any amount of symmetry in particle geometry or operating conditions. That high fidelity comes at a high computational cost, and as a result, TRISO particles are modeled in 3D sparingly. Most practical TRISO analyses that utilize BISON, particularly those involving failure probability predictions, are analyzed in 2D or 1D. 2D BISON simulations assume azimuthal symmetry, frequently referred to as *axisymmetry*, which uses quadratic elements to represent rings within the particle. 1D BISON simulations, on the other hand, assume complete spherical symmetry and use edge elements to represent spherical shells within the particle. The 3D model used in the previous section was modified to produce 2D and 1D models for further analysis in this section. Equivalent 3D and 2D computational domains and crack setups are shown in Figure 5.9 for comparison.

Note that, with the exception of the kernel, the element volumes and surface areas in the 3D model depend only on the distance from the particle center. In the 2D model, on the other hand, element volumes and surface areas vary with both the distance to the particle center and polar position (i.e., the angle at which a line connecting the element to the particle center intersects the axis of symmetry at the left side of the domain). 2D element volumes and surface areas are highest at the particle midplane and lowest at the top and bottom of the particle. Given that, a two-element-wide smeared crack oriented along the midplane of the 2D domain would have a different effective size than one oriented along its axis of symmetry. Additional simulations were run to investigate the potential impact on the flux-concentrating effects of cracks.

Five 2D cases were run with cracks oriented at 0° through 90° (downward along the axis of symmetry and rightward along the particle midplane). These are compared to a 3D case from previous sections and a 1D case utilizing the fully failed layer approximation. Release predictions are plotted in Figure 5.10. Therein, the 3D results have been multiplied

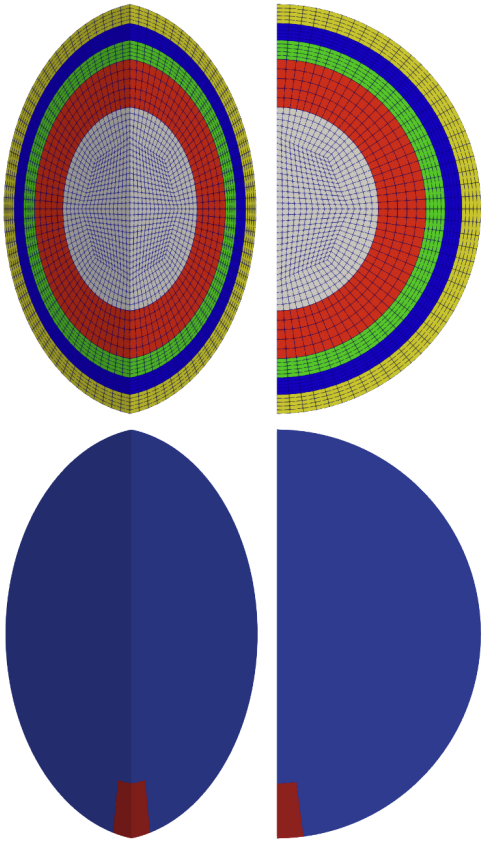

Figure 5.9. Equivalent 3D (left) and 2D (right) computational domains (top) and crack setups (bottom) used for additional multiphysics analyses.

by a factor of four to account for quarter-particle symmetry. All seven cases yield nearly identical results, as expected.

Local Pd fluxes through the cracks were then compared across the seven cases. Note that because the 1D model utilizes spherical symmetry and the fully failed layer approximation, the flux was taken from the entire inner IPyC surface. The results are plotted in Figure 5.10. Several points that need to be considered to properly interpret these results are discussed in the paragraphs below.

The results of the 2D case at 0° should be consistent with those of the 3D case, but there is a discrepancy between the two datasets. The element shapes and symmetry planes shown in Figure 5.9 hint at the source of the discrepancy. The 3D crack has a square cross section, whereas the 2D crack, when rotated about the symmetry plane, has a slightly smaller circular cross section. Correcting for the difference in crack areas yields consistent fluxes, as expected. The results of the 1D case should also be consistent with those of the 2D and 3D cases. Again, correcting for the differences in area yields consistent fluxes.

For the remaining 2D cases, the results show that flux decreases nonlinearly with increasing angle from 0° to 90°. This is consistent with the nonlinear increase in crack area with increasing angle through that range. As before, correcting for crack area yields consistent flux predictions, as expected. This discrepancy would need to be accounted for

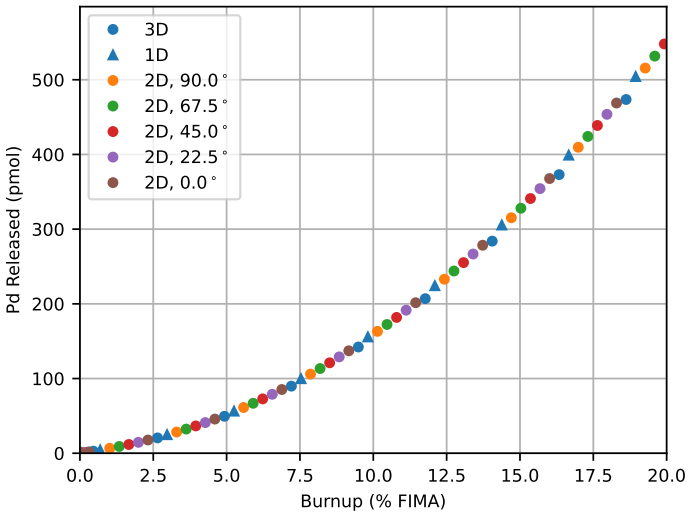

Figure 5.10. Pd release predictions obtained using a 3D model with a spatially resolved three-layer crack, a 1D model utilizing the fully failed layer approximation, and a 2D model with spatially resolved cracks in five different orientations.

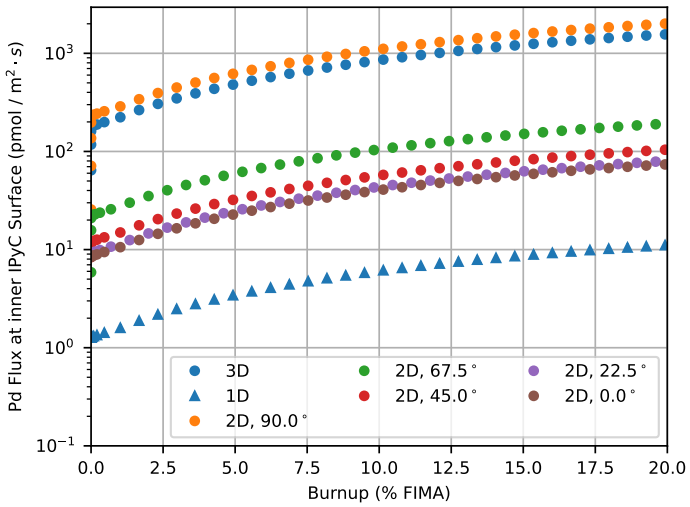

Figure 5.11. Crack Pd fluxes obtained from a 3D model, a 1D model, and a 2D model with cracks in five different orientations.

to properly capture the flux-concentrating effects that influence Pd penetration, but it may not be practical to implement this approach in a generally applicable Pd penetration modeling framework.

Overall, these results demonstrate that consistent release predictions can be obtained using all three dimensionalities. However, uncorrected flux predictions vary with dimensionality and with crack orientation in 2D. These two observations support using the fully failed layer approximation across dimensionalities for FP release predictions, and

an appropriate flux-concentration factor derived from atomistic calculations to capture realistic maximum Pd penetration depths when IPyC cracks are present.

5.7 Crack Timing

Finally, the 2D model introduced in the previous section was applied to assess the potential impacts of the timing of crack formation within a particle's lifetime. Three additional cases were run, introducing spatially resolved three-layer cracks at the 0° orientation and at burnups of 5, 10, and 15% FIMA. Release predictions from the three new cases are compared to results from the previous section in Figure 5.12. The results show that Pd released from the kernel prior to cracking is quickly released from the particle interior soon after the crack forms. The EOL release predictions are nearly identical. These observations suggest that treating cracks as fabrication defects is acceptable for overall release predictions when the total number of particle failures is already known, but that crack timing may be an important factor otherwise.

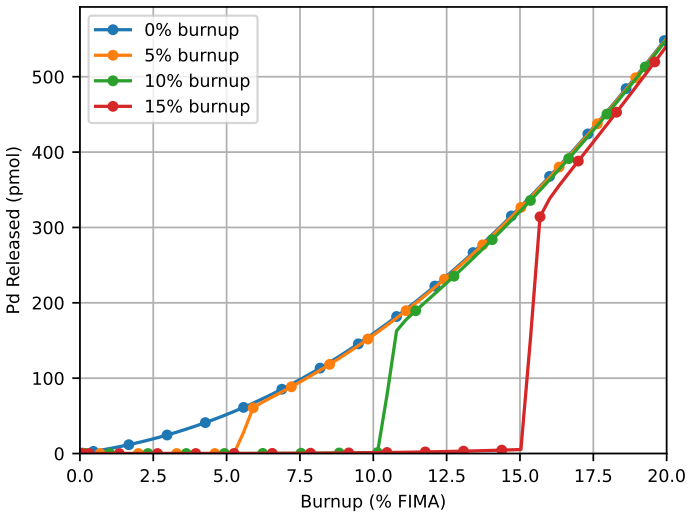

Figure 5.12. Pd release predictions obtained using a 2D model with spatially resolved three-layer cracks introduced at various burnups.

Flux predictions from the four cases are plotted in Figure 5.13. The results show that introducing cracks after the start of the irradiation produces momentarily higher fluxes as Pd that has already escaped the kernel is flushed from the particle. The flux through any crack then quickly converges to a value determined by the rate at which Pd continues to escape from the kernel. It should be noted that this rate increases with burnup. This is likely due to BISON's burnup-dependent Pd source term and the variable magnitude of the Pd concentration gradient at the kernel–buffer interface. These features may need to be taken into account when assessing realistic crack parameters at LLSs.

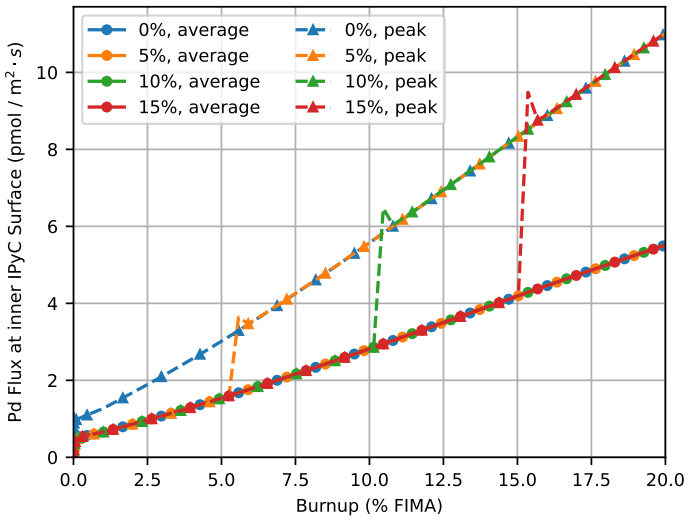

Figure 5.13. Pd fluxes through spatially resolved three-layer cracks introduced at various burnups.

5.8 Summary

Failure-statistics-informed, mesh-independent smeared cracking methods combined with the application of smeared, nonretentive diffusivities will provide a powerful, consistent tool set for modeling the dynamic behavior of tightly coupled multiphysics behaviors associated with particle failure. In this chapter, particles with various types of artificially induced cracks were simulated to assess the validity of the failure-related assumptions and simplifications frequently used in BISON, to make scientific observations to guide further research and model development, and to offer preliminary recommendations for how these models could be applied to support ongoing efforts to deploy TRISO-based fuels for commercial applications. Specifically, analyses were run to examine how crack formation and propagation, crack size, crack diffusivity, dimensional effects, and crack timing affect overall Pd release and local concentrations in Pd flux. General conclusions and recommendations for future work are summarized below.

Results showed that simulations conducted with both spatially resolved cracks and the fully failed layer approximation produce consistent release predictions. However, only the simulations conducted with spatially resolved cracks were able to capture the flux-concentrating effects of IPyC cracking, which may affect predicted maximum Pd penetration depth and therefore particle failure probability and subsequent FP release. Additional simulations were conducted to assess these behaviors under different conditions and to develop a flexible modeling approach that meets the needs of practical engineering applications and continued research and development.

Results also showed that crack formation and propagation can be neglected for most practical FP transport and release analyses. Release and flux behaviors depend not only on diffusivities in the various particle layers, but also on the relative magnitudes of those diffusivities. For example, a significant amount of Pd is retained within the kernel. Prior to cracking, Pd release is limited by both the kernel and the surrounding layers, whereas after cracking, release is limited only by the kernel. Care should be taken to take credit for FP retention in failed particles while maintaining an

appropriately conservative modeling approach. These observations emphasize the importance of using complete sets of accurate source terms and layer diffusivities for each FP of interest.

The analysis results also showed that smeared crack size affects flux but not release and that a sufficiently high smeared crack diffusivity can be applied to allow release of nearly all FPs that escape from the kernel. These results can be reproduced consistently across problem dimensionalities within the limits imposed by adopting azimuthal symmetry in 2D and spherical symmetry in 1D. Finally, we demonstrated that it is important to account for when, during a particle's lifetime, a crack occurs if the cumulative release from a population of particles is under consideration with an unknown number of failures, as is frequently the case. If it is desired to only know the EOL release amounts from a known number of particle failures, then the timing of crack formation is irrelevant.

Overall, the following approach is suggested. The fully failed layer approximation should be applied for release calculations, accounting for when cracking occurs in particle's lifetime, if at all possible. A flux-concentration factor should be applied within the Pd penetration model to account for local increases in flux when an IPyC crack is present to properly capture the maximum Pd penetration depth, failure probability, and overall release. The authors recommend that atomistic calculations be conducted with realistic crack dimensions to determine appropriate diffusivities and characterize expected crack throughput. Finally, dynamic smeared cracking models should continue to be applied to study these tightly coupled multiphysics behaviors for further research and development.

Future work in these areas may include:

- Calculating realistic surface diffusivities in retentive layers for application to cracks at the engineering scale, potentially accounting for anisotropy
- Conducting additional multiphysics analyses focused on characterizing FP transport in the presence of debonding and failure scenarios involving both cracking and debonding
- Updating and expanding BISON assessment cases according to the modeling approach identified above.

6. CONCLUSION

In this work, a framework for modeling Pd conservation in TRISO particles was developed. This included developing a model for Pd production within the kernel and applying diffusivities from the literature and ongoing LLS work at LANL to characterize Pd fluxes at the inner surface of the SiC layer. The analyses showed that, for a prototypic particle design and range of operating conditions, Pd flux is expected to be limited below about 1400 K and then increase rapidly with increasing temperature. Periods of low-temperature operation followed by periods of high-temperature operation may lead to higher transient Pd fluxes. This information was provided to the mesoscale team at INL to support the development of a mechanistic model for Pd penetration.

This work also leveraged new data and methods to improve BISON's general physical description of FP transport within TRISO particles. New buffer characterization data from the literature were used to calculate an appropriate surface density for use in the recently developed sorption mass transfer model at the buffer–IPyC gap. A preliminary model was then developed to simulate postulated FP trapping in the low-density buffer. Cs transport predictions were compared to particle-scale EPMA data from an AGR-2 particle with favorable results, providing proof of concept for a method of particle-scale validation that may reduce uncertainties compared to compact-scale validation using data from integral effects tests.

Next, we presented progress that has been made toward applying a smeared cracking approach to simulate the statistical, spatially resolved fracture of the SiC layer within TRISO particles. A methodology was developed to incorporate the statistical nature of the fracture strength into finite element simulations and validate this model using experimental measurements from hemispherical SiC crush tests. The next steps in this process involve developing a correction for mesh density and calibrating Weibull distribution parameters to deliver failure probabilities consistent with the crush tests and other available experimental datasets.

Finally, a series of multiphysics studies was conducted to assess the use of smeared, nonretentive diffusivities for the continued study of the tightly coupled multiphysics behaviors associated with particle failure. These studies may guide engineering applications leveraging these methods. Specifically, analyses were run to examine how crack formation and propagation, crack size, crack diffusivity, dimensional effects, and crack timing affect overall Pd release and local concentrations in Pd flux. Overall, the following approach is suggested. The fully failed layer approximation should be applied for release calculations, accounting for when cracking occurs in a particle's lifetime, if at all possible. A flux-concentration factor should be applied within the Pd penetration model to account for local increases in flux when an IPyC crack is present to properly capture the maximum Pd penetration depth, failure probability, and overall release.

High-impact future work in these areas may include:

- Assessing and developing models for Pd penetration at higher temperatures
- Considering more realistic time-varying irradation conditions to characterizing the effects of transient operation on Pd penetration
- Refining FP source term models by leveraging ongoing BISON–Griffin multiphysics coupling work being pursued under a collaboration between the NEAMS and AGR Programs
- Incorporating more realistic FP diffusivities into transport calculations as new experimental and/or LLS simulation data is made available
- Implementing user-friendly BISON models based on the dynamic smeared cracking methods demonstrated for SiC and extending them for use with other TRISO particle layers
- Updating and expanding BISON assessment cases to enhance consistency and incorporate the advancements described above.

Bibliography

[1] J.D. Hales et al. "Multidimensional multiphysics simulation of TRISO particle fuel". In: *Journal of Nuclear Materials* 443.1 (2013), pp. 531–543. ISSN: 0022-3115. DOI: https://doi.org/10.1016/j.jnucmat.2013.07.070. URL: https://www.sciencedirect.com/science/article/pii/S0022311513009586.

[2] Wen Jiang et al. "TRISO particle fuel performance and failure analysis with BISON". In: *Journal of Nuclear Materials* 548 (2021), p. 152795. ISSN: 0022-3115. DOI: https://doi.org/10.1016/j.jnucmat.2021.152795. URL: https://www.sciencedirect.com/science/article/pii/S0022311521000180.

[3] Wen Jiang et al. "Efficient high-fidelity TRISO statistical failure analysis using Bison: Applications to AGR-2 irradiation testing". In: *Journal of Nuclear Materials* 562 (2022), p. 153585. ISSN: 0022-3115. DOI: https://doi.org/10.1016/j.jnucmat.2022.153585. URL: https://www.sciencedirect.com/science/article/pii/S0022311522000812.

[4] G. Miller et al. *PARFUME Theory and Model Basis Report*. Report INL/EXT-08-14497 Revision 1. Idaho National Laboratory, 2018.

[5] Jason D. Hales et al. "BISON TRISO Modeling Advancements and Validation to AGR-1 Data". In: (Sept. 2020). DOI: 10.2172/1711423. URL: https://www.osti.gov/biblio/1711423.

[6] Jason D. Hales et al. "Numerical evaluation of AGR-2 fission product release". In: *Journal of Nuclear Materials* 558 (2022), p. 153325. ISSN: 0022-3115. DOI: https://doi.org/10.1016/j.jnucmat.2021.153325. URL: https://www.sciencedirect.com/science/article/pii/S0022311521005481.

[7] Jacob Hirschhorn et al. *Improved Fuel Particle and Compact Matrix Fission Product Release Prediction with Improved Mass Transfer Model*. Report INL/RPT-23-73972. Idaho National Laboratory, 2023.

[8] Somayajulu L.N. Dhulipala et al. "Bayesian uncertainty quantification of tristructural isotropic particle fuel silver release: Decomposing model inadequacy plus experimental noise and parametric uncertainties". In: *Journal of Nuclear Materials* 588 (2024), p. 154790. ISSN: 0022-3115. DOI: https://doi.org/10.1016/j.jnucmat.2023.154790. URL: https://www.sciencedirect.com/science/article/pii/S0022311523005573.

[9] P. Simon et al. "Mechanistic calculation of the effective silver diffusion coefficient in polycrystalline silicon carbide: Application to silver release in AGR-1 TRISO particles". In: *Journal of Nuclear Materials* 563 (2022), p. 153669. ISSN: 0022-3115. DOI: https://doi.org/10.1016/j.jnucmat.2022.153669. URL: https://www.sciencedirect.com/science/article/pii/S0022311522001635.

[10] Antonio M. Recuero, Gyanender Singh, and Wen Jiang. “Fracture mechanics approach to TRISO fuel particle failure analysis”. In: *Journal of Nuclear Materials* 596 (2024), p. 155083. ISSN: 0022-3115. DOI: https://doi.org/10.1016/j.jnucmat.2024.155083. URL: https://www.sciencedirect.com/science/article/pii/S0022311524001855.

[11] Eddie Lopez-Honorato et al. “Effect of Microstructure on the Resilience of Silicon Carbide to Palladium Attack”. In: *Journal of American Ceramic Society* 93 (12 2010), pp. 4135–4141. DOI: https://doi.org/10.1111/j.1551-2916.2010.04005.x. URL: https://doi.org/10.1111/j.1551-2916.2010.04005.x.

[12] Larry Aagesen et al. *Multi-scale fission product release model with comparison to AGR data*. Report INL/RPT-23-73761. Idaho National Laboratory, 2023.

[13] I. Karakaya and W. Thomposon. “The Ag-Pd (Silver-Palladium) system”. In: *Bulletin of Alloy Phase Diagrams* 9 (1988), pp. 237–243. DOI: https://doi.org/10.1007/BF02881271. URL: https://doi.org/10.1007/BF02881271.

[14] Han Liu et al. “A study of reaction between palladium, palladium silver alloy and silicon carbide ceramics at high temperature”. In: *Journal of the European Ceramic Society* 43.8 (2023), pp. 3077–3089. ISSN: 0955-2219. DOI: https://doi.org/10.1016/j.jeurceramsoc.2023.02.032. URL: https://www.sciencedirect.com/science/article/pii/S095522192300122X.

[15] E.J. Olivier and J.H. Neethling. “The role of Pd in the transport of Ag in SiC”. In: *Journal of Nuclear Materials* 432.1 (2013), pp. 252–260. ISSN: 0022-3115. DOI: https://doi.org/10.1016/j.jnucmat.2012.07.033. URL: https://www.sciencedirect.com/science/article/pii/S0022311512003923.

[16] David Petti et al. *Development Of Improved Models And Designs For Coated-Particle Gas Reactor Fuels*. Report INEEL/EXT-05-02615. Idaho National Laboratory for the International Nuclear Energy Research Initiative, 2004.

[17] Blaise Collin. *AGR-1 Irradiation Test Final As-Run Report*. Report INL/EXT-10-18097 Revision 3. Idaho National Laboratory, 2015.

[18] Blaise Collin. *AGR-2 Irradiation Test Final As-Run Report*. Report INL/EXT-14-32277 Revision 4. Idaho National Laboratory, 2018.

[19] Binh Pham et al. *AGR 5/6/7 Irradiation Test Final As-Run Report*. Report INL/EXT-21-64221. Idaho National Laboratory, 2021.

[20] Blaise Collin. *AGR-3/4 Irradiation Test Final As-Run Report*. Report INL/EXT-15-35550 Revision 0. Idaho National Laboratory, 2015.

[21] International Atomic Energy Agency. *WIMS Library Update Project: Fission product yields*. https://www-nds.iaea.org/wimsd/fpyield.htm#T2; accessed 1-Oct-2023.

[22] Nuclear Energy Agency Data Bank NEA. *JEF report 3 - table of simple integral neutron cross-section data from JEF-1, ENDF/B-V, ENDL-82, JENDL-2, KEDAK-4, RCN-3*. https://www.oecd-nea.org/dbdata/nds$_jeferreports/jefreport-3.pdf$; $accessed 1-Oct-2023$.

[23] J. Sterbentz. *JMOCUP as-run daily physics depletion calculation for AGR-3/4 TRISO particle experiment in ATR northeast flux trap*. Report ECAR-2753 Revision 1. Idaho National Laboratory, 2015.

[24] IAEA. *Fuel Performance and Fission Product Behaviour in Gas-Cooled Reactors*. TECDOC Series 978. Vienna: International Atomic Energy Agency, 1997. URL: https://www.iaea.org/publications/5633/fuel-performance-and-fission-product-behaviour-in-gas-cooled-reactors.

[25] Benjamin Liu. *Personal communication*. 9-Feb-2024.

[26] Karen E. Wright et al. "Fission product distribution in irradiated safety-tested and as-irradiated AGR-2 TRISO particles". In: *Journal of Nuclear Materials* 559 (2022), p. 153468. ISSN: 0022-3115. DOI: https://doi.org/10.1016/j.jnucmat.2021.153468. URL: https://www.sciencedirect.com/science/article/pii/S0022311521006887.

[27] A. Londono-Hurtado et al. "A review of fission product sorption in carbon structures". In: *J. Nucl. Mater.* 426.1 (2012), pp. 254–267. DOI: 10.1016/j.jnucmat.2012.02.019.

[28] Claire Griesbach et al. "A review of fission product sorption in carbon structures". In: *Journal of Nuclear Materials* 574 (2023), p. 154219. DOI: 10.1016/j.jnucmat.2022.154219.

[29] Y.R. Rashid. "Ultimate strength analysis of prestressed concrete pressure vessels". In: *Nuclear Engineering and Design* 7.4 (1968), pp. 334–344. ISSN: 0029-5493. DOI: https://doi.org/10.1016/0029-5493(68)90066-6. URL: https://www.sciencedirect.com/science/article/pii/0029549368900666.

[30] Ryan Terrence Sweet. "Thermo-mechanical analysis of iron-chromium-aluminum (FeCrAl) alloy cladding for light water reactor fuel elements". In: (2018).

[31] Brian C Davis et al. "Fracture strength and principal stress fields during crush testing of the SiC layer in TRISO-coated fuel particles". In: *Journal of Nuclear Materials* 477 (2016), pp. 263–272.

[32] Warren Clarence Young, Richard Gordon Budynas, Ali M Sadegh, et al. *Roark's formulas for stress and strain*. Vol. 7. McGraw-hill New York, 2002.

[33] Thak Sang Byun et al. *Fracture Stress Data for SiC Layers in the TRISO-Coated Fuel Particles*. Tech. rep. Oak Ridge National Lab.(ORNL), Oak Ridge, TN (United States), 2008.

[34] Seong-Gu Hong et al. "Evaluation of the fracture strength for silicon carbide layers in the tri-isotropic-coated fuel particle". In: *Journal of the American Ceramic Society* 90.1 (2007), pp. 184–191.